Potentiostat-Based Analogue Circuit for Wearable Glucose Sensors

A Low-Power Circuit Design For Continuous Sensing Applications

---

C.N. Guijt and J.J. van Ham

Potentiostat-Based Analogue Circuit for Wearable Glucose Sensors

A Low-Power Circuit Design For Continuous Sensing Applications

by

C.N. Guijt and J.J. van Ham

This thesis was written as part of the Bachelor's program in Electrical Engineering at TU Delft University of Technology. The project was conducted from April to June 2025 within the Faculty of Electrical Engineering, Mathematics, and Computer Science (EWI).

The work presented was done alongside a complementary project concerning the digital processing of the data generated by the sensor, as designed within this project.

We chose to do a project concerning continuous glucose monitoring due to our shared interest for the bio-medical field and analogue circuit applications.

We would like to thank the electrical engineering education staff for their dedication, kindness, and never-ending supply of coffee. Additionally, we would like to thank Filipe Cardoso for the great opportunity and advice. We would also like to thank Jeroen Bastemeijer and Flavia Valente for their meaningful contributions to the project.

C.N. Guijt

In particular, I would like to express my heartfelt gratitude towards two people who repeatedly ground *and* uplift me.

Thank you, İlke Ercan, for offering a safe haven in difficult times and situations. Your company and steadfast encouragement have often brought me the peace of mind, small joys, and realizations I needed to continue.

Thank you, Julian van Ham, for being a true friend. Even though, when we are not laughing, we love to argue ad infinitum. Your constant reliable presence has allowed me to keep functioning through difficult times. I truly treasure our shared brain-cell.

J.J. van Ham

My dad, for being my backbone, giving the best advice and dutifully attempting to read everything I will ever write. My mom, for making me dream big dreams. And Noah, for bringing cheer, love and rationality into my life, keeping me sane.

July 11, 2025

Supervisor:	Filipe Arroyo Cardoso
Project Duration:	April 2025 to June 2025
Faculty:	Faculty of Electrical Engineering, Maths, and Computer Science, Delft

Julian van Ham & Naomi Guijt

Abstract

The global prevalence of diabetes mellitus is rising rapidly, increasing the demand for reliable and accessible care. Current glucose monitoring solutions are often expensive, invasive, and uncomfortable, limiting their accessibility, especially in middle and low-income countries. This thesis presents the design of a compact, low-power, and continuous glucose monitoring (CGM) system with Bluetooth and separate electronics and sensor. The design integrates a potentiostat with a custom analogue pre-processing circuit, implemented on a printed circuit board (PCB).

The system supports Bluetooth Low Energy (BLE) communication for low-power wireless data transmission and is powered by a dual-coin-cell battery system designed for two weeks of operation. Furthermore, emphasis is placed on noise minimization and analogue-domain preprocessing to reduce power consumption, reduce measurement latency, and improve measurement accuracy. This was done with a trans-impedance amplifier, a non-inverting amplifier, and an integrator for signal conditioning. A classical potentiostat architecture was selected over more complex ASIC-based approaches for feasibility within the scope of the thesis.

Prototypes were tested using gold electrodes and phosphate-buffered saline with known analyte concentrations. Even though there were limitations barring full-system validation, the design demonstrates at least partial functioning and serves as a foundation for future refinement and integration. This work intends to contribute to the development of accessible CGM devices that balance clinical accuracy with real-world usability.

keywords: Continuous Glucose Monitoring (CGM), Bluetooth Low Power (BLE), Printed Circuit Board (PCB), Diabetes Mellitus (T1DM, T2DM), potentiostat, analogue filtering, wearable device

Contents

1 Introduction

This chapter introduces the context, motivation, and societal relevance of continuous glucose monitoring and outlines the key objectives and design criteria of the proposed system.

1.1 Purpose & Relevance

Research indicates that there will be 300-380 million adults with diabetes in 2025. Furthermore, Shaw et al. predict a worldwide increase in diabetics of more than 50% by 2030. This is a rapidly growing group of people in need of daily care. This care is heavily dependent on information on patients' glucose levels. This information is crucial for both the patient and their healthcare provider to make informed decisions regarding their care. [1]–[3]

However, glucose monitoring is inaccessible to most people suffering from diabetes. Firstly, measuring blood glucose directly by drawing blood poses the risk of infection. Secondly, the cost of continuous monitoring is often still too high for patients to afford. Thirdly, contemporary methods of continuous glucose monitoring still pose substantial discomfort, which discourages patients from treatment. Finally, to reduce the negative health impacts of diabetes as much as possible, measurements should also be reliable and easily usable. [4]–[6]

Moreover, in recent years, there has been increasing interest in user health electronics for sports. This has opened up another market for comfortable and easy-to-use glucose monitoring devices. These can help athletes not only monitor their daily performance and health, but in the future, these sensors could also be used to detect bio-markers for diabetes early in healthy adults without affecting daily function and comfort. [7], [8]

There is great potential for wearables as tools used by the general public. These tools can be used to monitor general health and optimize lifestyle decisions. [9]

1.2 Objectives

This design intends to combine several unique features in one product in order to address the points of section 1.1. These are

- Bluetooth functionality,
- Separated sensor and electronics,
- Miniaturized electronics,
- Analogue filtering, and
- Minimal Noise.

These features informed a program of requirements given in Chapter 3. Moreover, the analogue pre-filtering approach allows for unique predictive filtering methods, which could improve the quality of medical intervention (i.e., time and quantity for injection of insulin). [10]

2 Background

In order to design a simple and effective glucose monitoring device suitable for patients with Diabetes Mellitus, it is important that the underlying physical phenomena are well understood. In this chapter, the most important background information regarding the biological, medical, and technological front is explored.

2.1 Diabetes Mellitus

The primary market for the continuous glucose monitor (CGM) is that of people affected by Diabetes Mellitus. The monitoring of glucose allows patients to self-regulate their blood glucose levels using different health regimens.

Diabetes causes 5 million deaths worldwide yearly. 90% of these have senile diabetes (T2DM) in which the body becomes resistant to insulin. The other 10% has juvenile diabetes in which the body is unable to produce insulin. [10]

According to the World Health Organisation (WHO) 14% aged 18 and older in 2022 suffered from diabetes mellitus. Moreover, the treatment coverage was lowest in low- and middle-income countries, and more than half of the people with diabetes remain untreated. [4]

The WHO lists the primary symptoms of diabetes as:

- Feeling very thirsty,
- Needing to urinate more often than usual,
- Blurred vision,
- Feeling tired, and
- Losing weight unintentionally.

In addition, diabetes mellitus has many co-morbidities. E.g., over time, diabetes can damage blood vessels in the heart, eyes, kidneys and nerves.

T1DM; Juvenile Diabetes

Type 1 diabetes mellitus (T1DM) is an autoimmune disease that destroys insulin-producing pancreatic β-cells. T1DM is amongst the most prevalent chronic childhood illnesses, affecting approximately 1 in every 400–600 children and adolescents. [11]

Patients with T1DM must undergo complex and intrusive daily treatments. Invasive treatments can have negative impacts on quality of life. [12]

T2DM; Senile Diabetes

Type 2 diabetes mellitus (T2DM) is a metabolic disorder typified by a constant state of hyperglycaemia. In T2DM the body becomes unable to use insulin properly.

Senile diabetes is associated with a reduced life expectancy due to risk of heart disease, stroke, peripheral neuropathy, renal disease, blindness, and amputation.

In contrast with T1DM, T2DM cannot be treated using artificial insulin. However, though more prevalent in adults, the prevalence of T2DM is also on the rise in children and young adults. [4]

Monitoring

In short, glucose monitoring is an essential resource for diabetics which is not yet accessible to most prospective patients.

According to Ribet [10] there a three important considerations:

1. Damage is caused by large oscillations rather than constant hypo- or hyperglycemia. Therefore, it is important to measure consistently over time, not miss oscillations, and act quickly,
2. Regular pricking for direct blood glucose measurements (for the purposes of monitoring or calibration) exposes patients to a higher risk of infections, and
3. Pain and discomfort may often result in reduced patient compliance.

Thus, it is highly important to maximize the patient safety and comfort. For example, this can be done by reducing the size of the CGM and thereby the obstruction it poses. Or, reducing the amount of calibration points needed for accurate measurements can also improve patient safety

In order to achieve widespread distribution of care, the following requirements must be met:

1. Reduce the monetary cost,
2. Minimize the invasiveness and discomfort, and
3. Improve reliability.

2.2 Interstitial Fluid & Blood Glucose

Ribet [10] also stipulates the role of interstitial fluid (ISF), which makes up a quarter of the water contents of the human body and can be found in virtually any interstitial space in the body. In addition to water the ISF contains salts, glucose, small proteins, lipids, amino acids, fatty acids, hormones, neurotransmitters, and other small bio-molecules. The sensor that will be used will reach only the dermal layer of the ISF, therefore the dynamics between the blood glucose and ISF must be considered if one is to monitor the user's current glucose concentrations.

To this end digital processing will be applied after measurement. The digital processing is done according to a biochemical model of the dynamics between blood glucose and ISF glucose dynamics, enabling the determination of blood glucose concentration (BG). The mechanics and implementation of this model is outside of the scope of this design. [13]

2.3 Overview of electrochemical sensing

Electrochemical sensing is a technique to detect and measure the concentration of specific chemicals electrically. Fundamentally, it concerns an oxidation reaction at an electrode surface, resulting in an electrical signal that is proportional to the concentration of a specific substance, the analyte.

Some electrochemical processes require catalysts (e.g., enzymes) to take place, while others can occur independently. However, a forward voltage must be applied at an electrode to induce the oxidation of the analyte. This forward voltage is dependent on several factors, including the material of the electrode, the pH of the solution, and the analyte. [14]

Then, when the oxidation takes place, a current will be induced in the electrode from which the concentration can be inferred. This current is governed by the Cottrell equation, which relates the sensor and reaction characteristics to concentration. [15]

3 Program of Requirements

In this chapter, the specifications and requirements for the system are specified. The goals are separated into functional and technical goals. A functional goals specify the tasks and limitations that must be met or performed. A Technical goal is quantitative. These specify exact parameters (size, voltages, ranges, etc).

3.1 System Requirements

The current International Organization for Standardization (ISO) guidelines [16] require a ±20% resolution, when accounting for noise it would have a resolution limited ±5% but this can be eliminated by filtering. At therapeutic levels (i.e., higher than in average individuals) of AA and UA the have a maximum introduced error is lower than 2.5% from the sensor. Overall ISO 15197:2013 gives a minimum 95% accuracy which corresponds to ±15 mg/dl, meaning that at most the potentiostat circuit may introduce <2.5%.

For the electronics system the program of requirements is given by Table 3.1.

Functional	**Technical**
- Realizable in a relatively short time frame	- Deliver 500mV to electrochemical cell
- Minimal added error	- Deliver 5V to Bluetooth module
- Read out the sensor	- PCB maximum size of 40mm diameter
- Perform analogue filtering	- Less than 2.5% (±7.5mg/dLS) added error
- Transmit current value over Bluetooth	- Battery functional life-time of $\geq$2 weeks
- Rechargeable	- Wireless communication over $0 - 20$ meters
- Measure every one out of ten minutes	
- Store concentration values temporarily	

Table 3.1: Program of Requirements.

3.2 Sensor Specifications

In order to understand the requirements of the potentiostat circuit, first the Sensible sensor specifications must be understood. Ribet et al defined the sensor specifications as seen in Table 3.2. [17]

Functional	**Technical**
- Electrodes in ISF dermis layer	- Linearity up to 200 mg/dL
- Measure glucose as current	- Sensitivity of 27.2 nA/mg/dL
- Linear functionality in the relevant range	- Maximum current of 16.76nA
- Minimally invasive	- Reaction time of 10 mg/dL/min
- Non-harmful to the patient	- In vivo lifetime of two weeks

Table 3.2: Overview of sensor specifications by Ribet et al.

These restrictions will inform design decisions during the process. I.e., it must be considered whether a certain circuit can handle such small currents without great losses of accuracy and smallness.

In order to minimize the added error, there must be pre-processing steps. There are two very important steps to this: integration and filtering the noise. The integration has to take place over specific intervals to obtain the charge Q that is the solution to the integral of the Cottrell equation without interference from other charges.

3.3 Overview

In the following section an overview of the system is shown and explained. The overview of the analogue processing stages are shown in the diagram in fig 3.1.

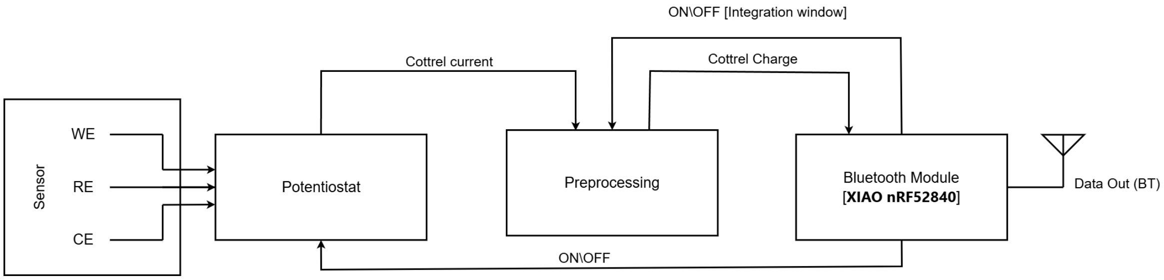

Figure 3.1: Block diagram of the implementation of the system.

Firstly, there is the sensor block containing the electrodes. With these electrodes the Cottrell currents are measured in the electrochemical cell. The electrodes are connected to the potentiostat with which their potential is enforced and the out coming current is amplified. More information about the sensor can be found in Section 4.4.

Then, The potentiostat stage. This stage must ensure certain electrical conditions in the sensor are enforced such that sensing can take place. Moreover, it amplifies the resulting current before passing that to the preprocessing stage. This stage can be turned off by the microcontroller when not measuring. This stage is further elaborated upon in Chapter 5.1.

Then, the preprocessing stage. In the preprocessing stage all signal conditioning and filtering steps are contained such as filtering, further amplification, and integration. The preprocessing stage can also be deactivated by the microcontroller. Specifically, this is done at the integrator such that the microcontroller can control the integrator charging and discharging behaviour. After preprocessing the Cottrell current is integrated, thus the Cottrell charge is passed to the microprocessor. This is elaborated upon in Section 5.2.

Finally, the microcontroller is the communication and control unit of the circuit. This stage can control the other stages for measurements and transmit the measured data wirelessly. The microprocessor also stores data in case a connection cannot be established. Moreover, this stage also includes the power source (i.e., removable rechargeable batteries) with which the rest of the system is powered. More information about the microprocessor and power supply can be found in Chapter 4.

4 Hardware Platform

4.1 Microcontroller

For the microcontroller the most critical feature is the size, ideally, the processor used should be only as large as the sensor ($\leq$ 20mm). Moreover, the wireless transmission should consume as little power as possible in order to conserve battery charge. To this end, the selected processor is *Seeed XIAO nRF52840* as seen in fig 4.1. This is a microprocessor with extremely low sleeping current usage (5μA) and small surface area. Moreover, it has built-in low-power Bluetooth functionality, 256 kilobytes RAM, and two megabytes onboard Flash.

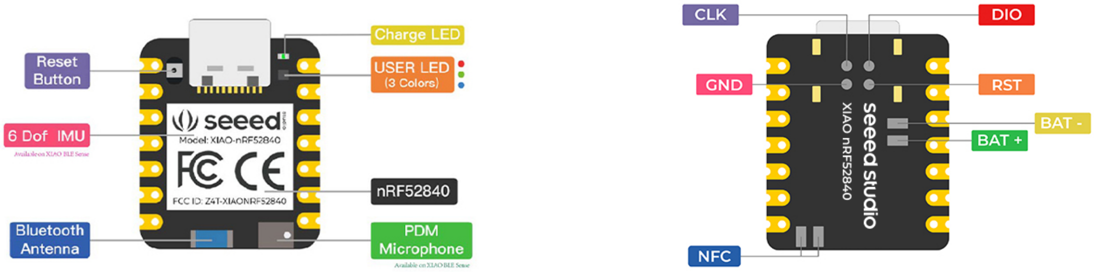

Figure 4.1: XIAO nRF52840 Sense front and back indication diagram

The board has 6 ADC analogue input pins where outputs from the potentiostat can be digitalized and transmitted. These six pins expect a voltage from 0-3.3V (which gives another technical specification for the output signal).

In testing the ADC ports are reliably linear as seen in Fig 4.2. As a result, no external ADCs required.

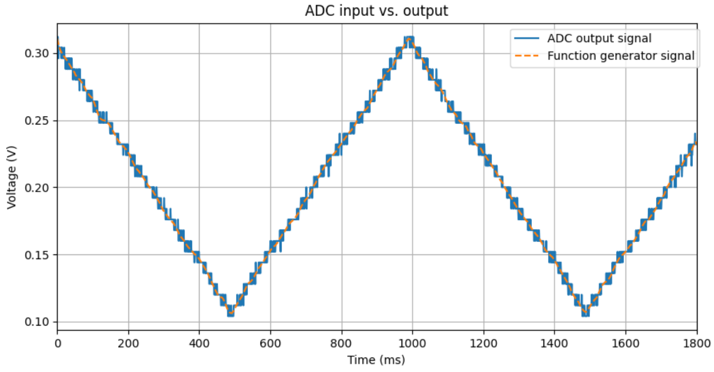

Figure 4.2: ADC output vs. input for 0.1 - 0.3V such that the quantization levels can be seen

4.2 Battery & Power management

For power management, several things must be accounted for

- Voltage drop related brownouts,
- Maximal continuous current,
- Total capacity, and
- Rechargeability.

The processor supports multiple different modes of transmission. It can achieve different ranges of communication at different levels of power and current consumption.

The bottleneck limitation is the current requirements for Bluetooth transmission. The microprocessor mentioned above has two voltage input ports with different limitations. Importantly, the VBUS (5V) input requires a lower current for transmission.

4.2.1 Battery

For this reason two 3 volt batteries with 220 mAh each were selected giving a total of 6 volts and 440mAh (I.e., CR2032). This gives the maximal total continuous current in Equation (4.1).

$$\frac{440[mAh]}{24[h] \cdot 14[days]} = 1.3[mA] \tag{4.1}$$

However, because the measurements will take place for one out of every ten minutes, the maximal continuous discharge may be as high as 11.8mA. The sensor will only be turned on for 11% (10% with 1% margin)of the 336 hour lifetime. To turn minimize power outside of operation, the MCP6004 is connected to the battery via a MOSFET switch controlled by the microcontroller.

$$\frac{440[mAh]}{24[h] \cdot 14[days] * 0.11} = 11.8[mA] \tag{4.2}$$

Thus there should be enough current to allow for all ICs including the microprocessor to function correctly during active periods if the power consumption is assumed to be negligible in the inactive periods. Note that the actual battery-life time is found in Section 5.3.6 to be 26.5 days due to power draw from the integrated circuits and efficiency of the voltage regulator.

4.2.2 Voltage Regulator

Due to the requirements of the Xiao microcontroller (and other ICs typical requirements) a voltage regulator is required to transform the 6V input into a 5V output to the circuit. For this reason a simple 5V voltage regulator was used. The circuit can be seen in fig 4.3.

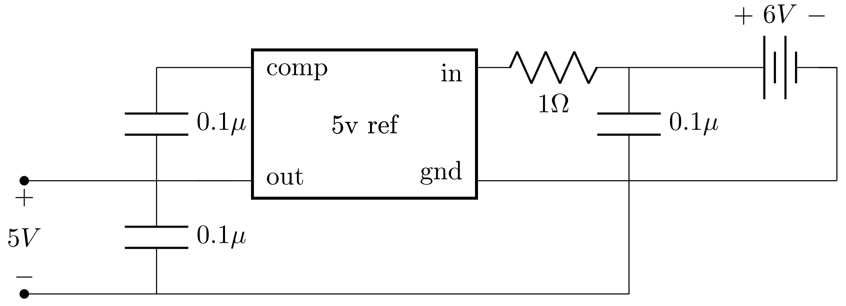

Figure 4.3: Circuit for battery and 5V reference output to circuit

Where values for coupling capacitors and input impedances were chosen according to component reference sheet [18].

4.3 Wireless Communication

For the wireless communication capabilities the Bluetooth protocol was selected because of its appropriate communication range and the broad compatibility with user devices. Moreover, the Xiao microcontroller that is being used for this implementation of the design has built in low power Bluetooth (BLE) functionality.

4.3.1 Limitations

The Xiao Bluetooth module is configurable from -20 dBm to +8 dBm, in 4 dB steps. In order to estimate a range for BLE in real world situations where there is interference from external sources. Moreover, the throughput of the system is greatly affects and is affected by the range, being significantly dependent on the bit error rate (BER) [19]. Based on this we can estimate considering inside and outside conditions that we have ranges as seen in table 4.1. [20]

Current Requirements	Power	Range
14.8 mA	+8dBm	30-40m
9.6 mA	+4dBm	20-30m
4.8 mA	+0dBm	10-20m
3.1 mA	-4dBm	<10m

Table 4.1: Xiao microcontroller BLE ranges over different power requirements.

Based on this, the 4.8mA and 3.1mA modes are most appropriate as the maximal current at any one time should be less than 6mA and according to the aforementioned requirements the aim is to have communication at a range up to 20 meters.

4.4 Sensor

In order to achieve a minimally invasive sensor as specified in Section 3.2, nano-scale sensors are used. These sensors allow for nano-scale needles that minimize discomfort for patients and risk for infection like with pricking blood.

Specifically, the design hereafter is intended to be used with the electrodes as outlined in the 2018 paper by Ribet et al. The sensor proposed therein has an order of magnitude of micrometers. In Figure 4.4 and Figure 4.5, the sensor and electrodes are shown. As the magnitude of the measured current is proportional to the surface area of the electrodes, this will inform the design.[21]

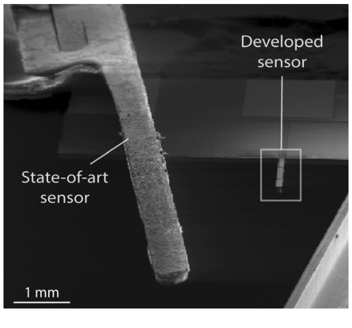

Figure 4.4: SEM image comparing the sensor realized by Ribet et al., compared with a state-of-the-art device (Abbott Freestyle Libre). [21]

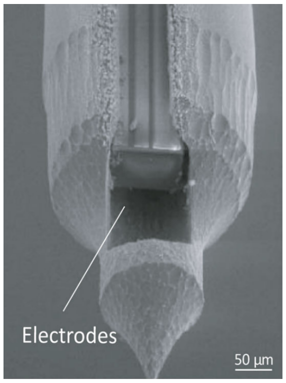

Figure 4.5: Close-up view of the microneedle opening. For visualization purposes, the opening has been enlarged by laser ablation to display the three-electrode sensor inside the microneedle lumen. [21]

5 Circuit Design

5.1 Potentiostat

The potentiostat is an electronic sensor which measures and controls the voltage difference between two electrodes, the working electrode and the counter electrode. The potentiostat typically functions according to a cyclic voltammogram. Meaning that there is a certain potential for which the forward (oxidation) half-reaction takes place at the working electrode, and some reverse energy for which the reverse (reduction) half-reaction takes place at the counter electrode. From the voltametric results physical properties can be determined (i.e., the glucose concentration).

5.1.1 Mechanism

The most common potentiostat configuration is a three electrode system consisting of a working electrode (WE), counter electrode (CE), and reference electrode (RE) or a pseudo-reference electrode (RE). The potentiostat circuit as shown figure 5.2 serves to enforce a potential difference between the working (WE) and counter electrode (CE). Ideally, this is achieved with minimal loss caused by the medium between the electrodes. This loss is called the Ohmic drop (IR). Positioning the reference electrode closer to the working electrode will lower the Ohmic drop [22].

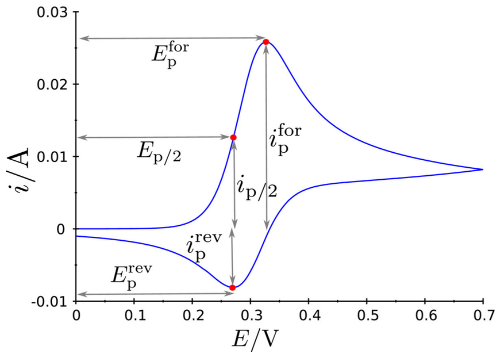

Figure 5.1: Example cyclic voltammogram by Bogdan et al [23]. Including the forward peak, half peak, and reverse peak potentials.

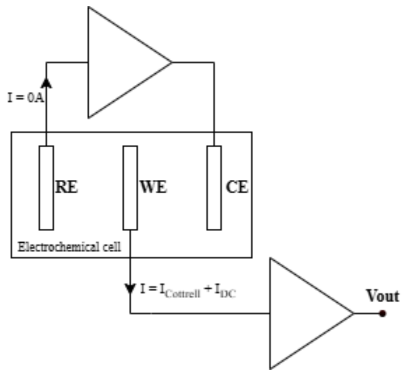

Figure 5.2: Schematic drawing of the simplified circuit diagram for a three-electrode potentiostat system.

The enzymatic mechanism specifically relevant in this work is that of glucose oxidase (GOx) as seen in Equation (5.1). This reaction supplies the hydrogen peroxide molecules needed for the oxidation half-reaction seen in equation (5.2), which takes place at the working electrode [21].

$$\mathrm{Glucose} + \mathrm{O_2} \xrightarrow{\mathrm{GOx}} \mathrm{Gluconic\ Acid} + \mathrm{H_2O_2} \tag{5.1}$$

$$\mathrm{H_2O_2} \xrightarrow{500\,\mathrm{mv\ \ vs.\ IrOx}} 2H^+ + O_2 + 2e^- \tag{5.2}$$

while at the counter electrode the current flow is balanced by the reduction reaction [17]:

$$2\,\mathrm{H^+} + 0.5\,\mathrm{O_2} + 2\,\mathrm{e^-} \longrightarrow \mathrm{H_2O} \tag{5.3}$$

The oxidation reaction at the working electrode in equation (5.2) requires that there is a $500mV$ potential drop from the working electrode to the reference electrode [21]. Moreover, Ribet et al [21] gives specifications for the electrode composition:

> **Working Electrode.** Platinum (Pt) electrode biased with 500mV with reference to the pseudo-reference. Because the GOx mechanism requires oxygen, there must be an abundance of oxygen at the working electrode.
>
> **Pseudo-Reference Electrode.** Integrated iridium oxide (IrOx). Compared to a commercial Ag/AgCl reference electrode the Iridium Oxide psuedo reference was confirmed by Ribet et al to perform satisfactorily.
>
> **Counter Electrode.** Platinum (Pt) electrode responsible for closing the electrical circuit.

Ribet et al, have realized several topologies and areas for the potentiostat probe. The process of cyclic voltammetry was used, to form the oxide layer on the iridium pseudo-reference electrode.[10]

The potential measured by the potentiostat is dependent on the diffusion of molecules in the substrate (i.e., the ISF). This diffusion typically takes place in regions as seen in figure D.1. These regions are the compact layer, diffuse layer, and diffusion layer. Because the potential measurements are dependent on the ions located in the compact layer, the concentration of the oxidized molecules in the bulk has to be extrapolated from the concentration at the electrode surface.

5.1.2 Circuit

Requirements

The potentiostat serves two central purposes. It must enforce a 500 mV potential over the WE-RE electrode and measure the charge resulting from the electrochemical process.

To achieve this, the following properties of the circuit are important:

- The current passing CE must equal WE; By extension, the current into RE must be zero amperes,
- charge generated by the chemical process must be amplified and supplied to the pre-processing blocks, and
- Power usage must be minimal.

Thus, a circuit must be designed with a feedback loop which will make the value at the RE electrode must always oscillate closely around the selected value (i.e., $500mV$). Then at the output (The WE electrode) there is a transimpedance amplifier that turns the output current into a voltage with a gain factor $G = -R_f$. This output voltage V_{out} will then be integrated by the integrator and passed to the Kalman filter in order to make predictions. These implementations can be seen in fig 5.3

Decision-Making

For the potentiostat there are many possible implementations. Many novel methods for these implementations have great advantages in power or precision. However, most of these implementations are done with an application specific integrated-circuit (ASIC) and have a great depth requiring more time to fully explore. Due to time constraints, ASIC was not within the scope of the design. For future works and transparency an overview of options that were considered at the exploratory stage are given below

The **classic** design denotes the fundamental potentiostat. That is, a circuit as described in fig **??**. This circuit can be readily implemented using ICs and analogue components. Typically this is a more simple but reliable implementation. [24]

The **current mirror** architecture works similarly to the classic implementation but the measured current is measured via mirrored current. This way at the cost of introduced error, power can be conserved. This would be implemented with an ASIC. [25]

The **chopper with fully differential architecture** is an implementation with a different structure than the classical implementation. Here a differential architecture enforces a lower voltage at the RE electrode, which causes the forward reaction at the WE electrode. This architecture allows for more precision in control and measurement but is more costly in terms of power. This can be done with ICs and as ASIC. [26]

The **digital regulation loop** is the most unique application where the potentiostat is implemented without amplifiers. This is a unique method that allows for low power consumption and high precision but it is also difficult to implement and highly complicated. This can only be reasonably implemented as ASIC. [27]

In table 5.1 the features of the possible implementations are compared and contrasted.

Criteria	**Classic**	**Current Mirror**	**Chopper**	**Digital**
Size (non-ASIC)	+2	-2	-2	-2
Feasibility (scope)	+2	-1	-1	-1
Low noise	0	+1	+2	+1
Power usage	-1	+2	0	0
Resolution	0	0	+1	+1
Control precision	0	0	+1	0
Simplicity	+1	-1	-2	-2
Total	*+4*	*-1*	*-1*	*-1*

Table 5.1: Harrison decision profile for proposed stages of the pre-processing circuit. Here positive score represents a positive effect (i.e., a '+1' for power usage means the stage is low power). Ordered from most to least important.

Thus, given that an ASIC implementation is no within the scope of this design, the classic implementation of the potentiostat is the most appropriate choice of architecture.

Implementation

The fundamental mechanism for the implementation of this circuit is a feedback loop. To satisfy the requirements given above, a simple operational amplifier suffices. Thus, one is placed between RE and CE such that the current in the reference is zero and both RE and CE are driven to have a zero potential. A resistor at the output of this amplifier is added to increase stability in this feedback loop.

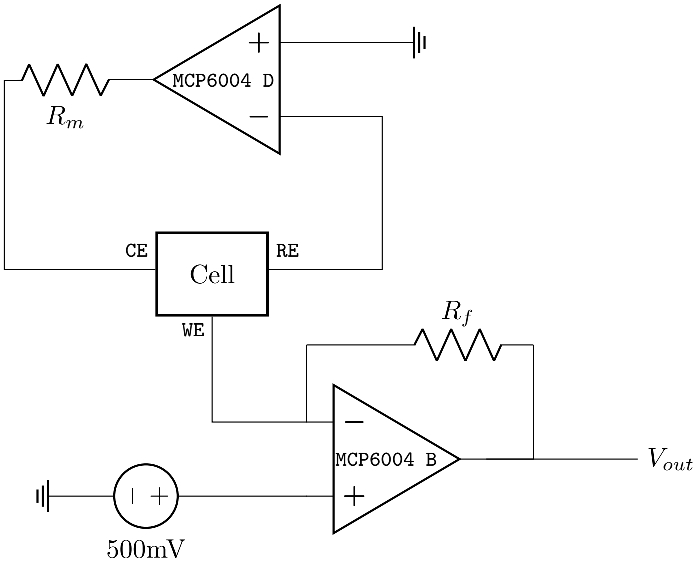

Figure 5.3: Schematic for Potentiostat.

At the other electrode, WE, 500mV is forced by a transimpedance amplifier which converts the current resulting from the electrochemical process in the cell into a voltage that can be integrated over by the integrator. The circuit was thus designed as seen in Fig 5.3.

5.2 Pre-processing

5.2.1 Requirements

The analogue pre-processing circuit has several important purposes. These are

- Amplify the output of the potentiostat,
- Integrate the value to find the charge, and
- Contain noise within set specifications.

To achieve this, several key requirements must be met.

Based on the nano-scale of the surface area of the electrodes on the sensor, an order of magnitude of 10^{-9} was assumed for the output current of the potentiostat. Accordingly, the cumulative gain of the pre-processing stages should lift this magnitude to a scale of 10^{-1} to 10^{-2} to be digitized at the ADC.

Furthermore, the signal must be integrated without saturating too quickly. If the signal does saturate, information is lost. Moreover, the charging time should be appropriate for the window in which the measurement is done.

Finally, when choosing values in the pre-processing stage, these must not be too large. Large impedances induce greater noise, especially those in feedback paths, as these paths are amplified even further.

5.2.2 Decision-Making

Initially, three potential stages with different purposes were proposed for pre-processing. These are

- Integrator,
- gain stage,
- passive fitering, and
- Kalman filter.

Firstly, the current should be integrated to obtain the charge, this can be done digitally or analogue, but in the analogue domain it costs less time. Secondly, an amplification stage would be useful to amplify the signal such that the complete range of the ADC can be utilized. Finally, a Kalman filter would allow for minimum error filtering and predictive capability in order to minimize time delay between the actual blood glucose concentration and the read value. [28]

Criteria	**None**	**Integrator**	**Gain-stage**	**Kalman filter**	**Passive filter**
Noise filtering	-1	+1	+1	+2	+1
Size (small)	+1	-1	0	-2	+2
Resolution	-1	0	+2	0	-2
Power usage	+2	-1	-1	-2	0
Usability	-2	+2	0	+2	-2
Simplicity	+2	+1	+2	-2	+2
Total	*+1*	*+2*	*+2*	*0*	*+1*

Table 5.2: Harrison decision profile for proposed stages of the pre-processing circuit. Here positive score represents a positive effect (i.e., a '+1' for power usage means the stage is low power).Ordered from most to least important.

Based on the total value of the columns of the decision matrix seen in table 5.2 it can clearly be seen that the largest positive impact is given by the gain stage and the integrator stage.

Thus, to minimize the error and noise to within the specified limit (2.5% added error at the output) the integrator and amplification are implemented to reduce noise.

5.2.3 Integrator Mechanism

The Cottrell equation which describes the current flowing out of the potentiostat at forward potential is given in Equation (5.4).

$$I(t) = \frac{nFAD^{1/2}C_0}{\pi^{1/2}t^{1/2}} \tag{5.4}$$

For digital processing, it is good to consider the integral form of the Cottrell equation as seen in Equation (5.5). This is done because the relevant signal frequency spectrum is smaller than the noise spectrum, therefore the integrator acts as a sort of low-pass filter which excludes high-frequency noise from the calculations hereafter.

$$Q_{avg} = \frac{1}{T}\int_0^T \frac{nFAD^{1/2}C_0}{\pi^{1/2}t^{1/2}} \tag{5.5}$$

It is very important to consider the correct integration window size as this directly impacts the quality of the signal-to-noise ratio (SNR). After the window of integration has passed, the value is held by the microprocessor and transmitted or stored.

The integration is done in the analogue domain for two important reasons: it will cost less time to filter in analogue domain and will reduce the amount of data that must be transmitted over the wireless connection (n.b. wireless transmission has the highest power cost per unit time of all circuit operations). Therefore, this is highly beneficial in power consideration and calculation time.

5.2.4 Integrator Circuit

Requirements

The integrator circuit is intended to find the integral of the current measured over the output of the WE electrode such that the total charge can be found. There are two important factors to consider for this:

- Integration window,
- On / off switching, and
- Saturation.

That is, it must be possible to select a window by switching the integrator on and off. Moreover, the window must be selected well as this greatly affects the SNR. Thus, values for the passive components must be chosen accordingly as the output could saturate if the time constant is too short and the capacitor is charged fully too quickly.

Implementation

The circuit used to implement the intended functionality specified in the last section can be seen in Figure. An image of the circuit is shown in 5.4.

In Appendix C circuit analysis is used to find expressions for the output voltage when integrating or discharging.

5.2.5 Amplification stage Circuit

Requirements

The amplification stage has two requirements. First, is must be able to implement a gain somewhat flexibility. This is to allow the gain-factor to be changed should the requirements change retroactively. Secondly, the topology should be non-inverting. This is important since the trans-impedance amplifier and integrator are both inverting.

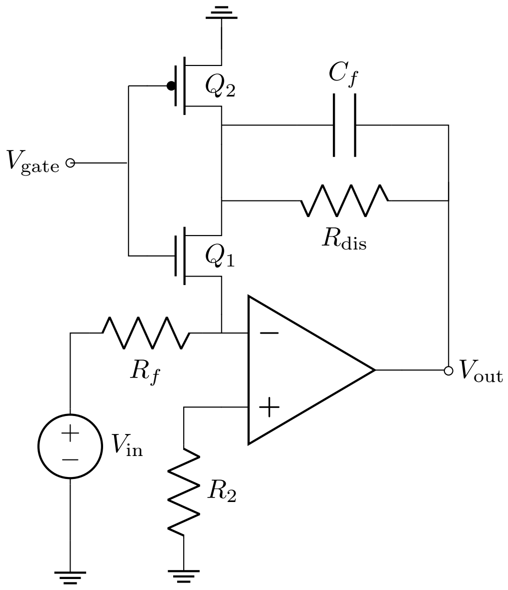

Figure 5.4: Integration Circuit Schematic.

Mechanism

The gain of the trans-impedance amplifier $A_{\text{trans.imp}}$ is calculated in Appendix A with Equation (5.6).

$$A = R_f \tag{5.6}$$

A resistor valued at $R_f = 22k\Omega$ is selected. Which gives an amplification of $22k$.

The gain of the integrator is calculated in a similar fashion in Appendix C. This gain is bound by the physical size of the capacitor C_f and the time-constants calculated in the same appendix. In Appendix C Equation (5.7) was found.

$$A_{\text{int}} = \frac{1}{R_1 C_f} \tag{5.7}$$

Lastly, the gain of the gain stage is found in Appendix B as:

$$A_{\text{gain}} = 1 + \frac{R_a}{R_b} \approx \frac{R_a}{R_b} \tag{5.8}$$

Combining gains (5.6), (5.8), (5.8) with the gain requirement (5.14) in Equation (5.14) gives:

$$R_f \cdot \frac{1}{R_1 C_f} \cdot \frac{R_a}{R_b} = 2 \cdot 10^9 \tag{5.9}$$

Using $R_f = 220k\Omega$, $R_1 = 220k\Omega$, and $C_f = 22\mu F$ it can be found that:

$$\frac{R_a}{R_b} = 22k\Omega \tag{5.10}$$

So, a resistor $R_a = 22k\Omega$ and $R_b = 1\Omega$ were selected to full-fill the gain target.

5.3 Design Consideration

5.3.1 Voltage Regulators

As previously clarified in section 4.2, a shunt voltage regulator is used to supply the ICs with a supply voltage of 5 volts. Moreover, a precise low-voltage reference is used to set the forward voltage.

These were used instead of voltage dividers to conserve power, as voltage dividers consume power continuously, especially directly at the output of the battery. In Equation (5.11), the power relation of the voltage divider is highlighted.

$$P_{divider} = P_{R_1} + P_{load} + P_{R_2} \tag{5.11}$$

$$= {I_{R_1}}^2 \cdot R_1 + \frac{{V_{load}}^2}{R_{load}} + {I_{R_2}}^2 \cdot R_2 \tag{5.12}$$

Thus, we can characterize the efficiency as in Equation (5.13).

$$\eta_{divider} = \frac{P_{load}}{P_{total}} = \frac{{V_{load}}^2}{R_{load}(R_1 \cdot {I_{R_1}}^2 + R_2 \cdot {I_{R_2}}^2) + {V_{load}}^2} \tag{5.13}$$

As the regulators are designed for low power functioning, it is a valid assumption that $\eta_{\text{regulator}} \gg \eta_{\text{divider}}$. Moreover, the efficiency of a divider is dependent on the impedance of the load and the current drawn, which are not reliable for specifying power consumption. Thus, voltage regulators were used.

5.3.2 Integrator Time-Constant

In Appendix C the time-constant of the integrator was found as $\tau = C_f R_f$. This introduces a constraint on the values of these components. Pol and Menkveld [29] specified a maximal integration window of one minute. Therefore, $47\mu F$ and $220k\Omega$ were selected. These values give a maximal charging window of $51.7[s]$.

5.3.3 Gain Constraint

One of the requirements for the pre-processing is to take the current output from the cell, into the range of the microcontroller ADC. The ADC has a fixed range of $0V - 3.3V$. If it is assumed that the output current of the chemical cell is in the nano-ampere ranges the gain needed can be calculated as:

$$A_{\text{req}} = \frac{2V}{100 \cdot 10^{-9} A} = 20 \times 10^6 \tag{5.14}$$

via the product of all the series amplifications; corresponding to the trans-impedance amp A, integrator C and gain stage **??**. This equation is given as Equation (5.15).

$$A_{\text{trans.imp}} \cdot A_{\text{gain}} \cdot A_{\text{int}} = A_{\text{req}} \tag{5.15}$$

Thus we must find an amplification factor A_{gain} which results in a total cumulative amplification of 10^9. The amplification of the integrator stage was justified in Appendix C as Equation (5.16).

$$A_{\text{int}} = \frac{1}{R_f C_f} \tag{5.16}$$

Using the values necessitated by the time-constant, the amplification factor is found to be $A_{\text{int}} = 0.09$. The gain stage and trans-impedance amplifier must therefore exhibit a combined gain of $A_{\text{gain}} \cdot A_{\text{trans,amp}} = 0.22 \times 10^9$. A trans-impedance gain of $22k$ and a non-inverting gain of $10k$ and are used for a total gain of 0.22×10^9. These gains are implemented via a two feedback resistors $R_f = 22k\Omega$ and $R_a = 10k\Omega$.

5.3.4 Coupling Capacitors

The circuit features numerous coupling capacitors. DC-coupling is added to add reliability to the power-supply of the MCP6004. The data-sheet [30] specifies that a $0.1\mu F$ capacitor should be placed within 2mm of the input terminal. Additionally, an AC-couple is added between the output of the trans-impedance amplifier and the input of the amplifier. The goals is to filter the signal of the $500mV$ bias. Discussion of the origin of the bias can be found in Appendix A.

5.3.5 Noise

The total noise factor is given by

$$F_{\text{total}} = F_1 + \frac{F_2}{G_1^2} + \frac{F_3}{(G_1G_2)^2} + \frac{F_n}{(G_1G_2\cdots G_n)^2} \tag{5.17}$$

Doing this calculation with gains and input-referred noise densities found in Appendices A, B, C gives a final input referred system noise of $57.3[nV/\sqrt{Hz}]$. This noise fits within the technical specification of 2.5% error under the condition that:

$$\frac{57.3[nV/\sqrt{\text{Hz}}]\cdot\sqrt{B}}{57.3[nV/\sqrt{\text{Hz}}]\cdot\sqrt{B}+I_{RMS,in}} \leq 0.025 \tag{5.18}$$

The integrator topology with the chosen values will have a cut-off frequency of $f_c = (2\pi R_f C_f)^{-1} = 0.014[\text{Hz}]$.

Entering this into Equation (5.18) gives a maximal RMS input current of

$$I_{\text{RMS,min}} = 8.36[nA] \tag{5.19}$$

This result is satisfactory, as it was earlier assumed that the output current of the cell would be in the $100[nA]$ range. [10].

5.3.6 Power

The main consumption happens in the MCP6004. All passive components can be shown to have a negligible power consumption (μW range). To simply calculations, only the quiescent current of the MCP6004 and the power-usage of the Xiao microcontroller is considered. The MCP6004 has a quiescent current of $100mA$/amp [30]. The Xiao microcontroller has a sleep-mode with a current draw of $5\mu A$ and an active current consumption of $4.8mA$. The average power consumption of the MCP6004 and Xiao with a 11% on-time given in Equations (5.20) and (5.21).

$$I_{\text{XIAO(avg)}} = 0.11\cdot 4.8[mA] + 0.89\cdot 5[\mu A] = 0.53245[mA] \tag{5.20}$$

$$I_{\text{MCP(avg)}} = 0.11\cdot 0.4[mA] + 0.89\cdot 0[\mu A] = 0.044[mA] \tag{5.21}$$

Using these values the maximal lifetime of the battery is given Equation (5.22).

$$T = \frac{0.833\cdot 440[mAh]}{0.576[mA]} = 635.9[h] = 26.5[\text{days}] \tag{5.22}$$

From this it is calculated in Equation (5.23) that the minimum capacity possible to sustain this circuit for 336 hours is 193.5 mAh.

$$0.576[mA]\cdot 336[h] = 193.5[mAh] \tag{5.23}$$

6 Realization & Testing

This chapter presents the realization and testing of the circuit designs using both hand-soldered prototypes and a final printed circuit board (PCB) created in KiCad 9.0. Key components, including the integrator, were individually validated and later integrated into the complete system, which demonstrated correct functionality during testing. Whereas passive elements were justified in chapter 5, the active elements used will be described and justified in the following.

6.1 Schematic

The circuits as described in chapter 5 about the design were integrated and compiled in KiCad 9.0. The complete circuit can be seen in Figure 6.1.

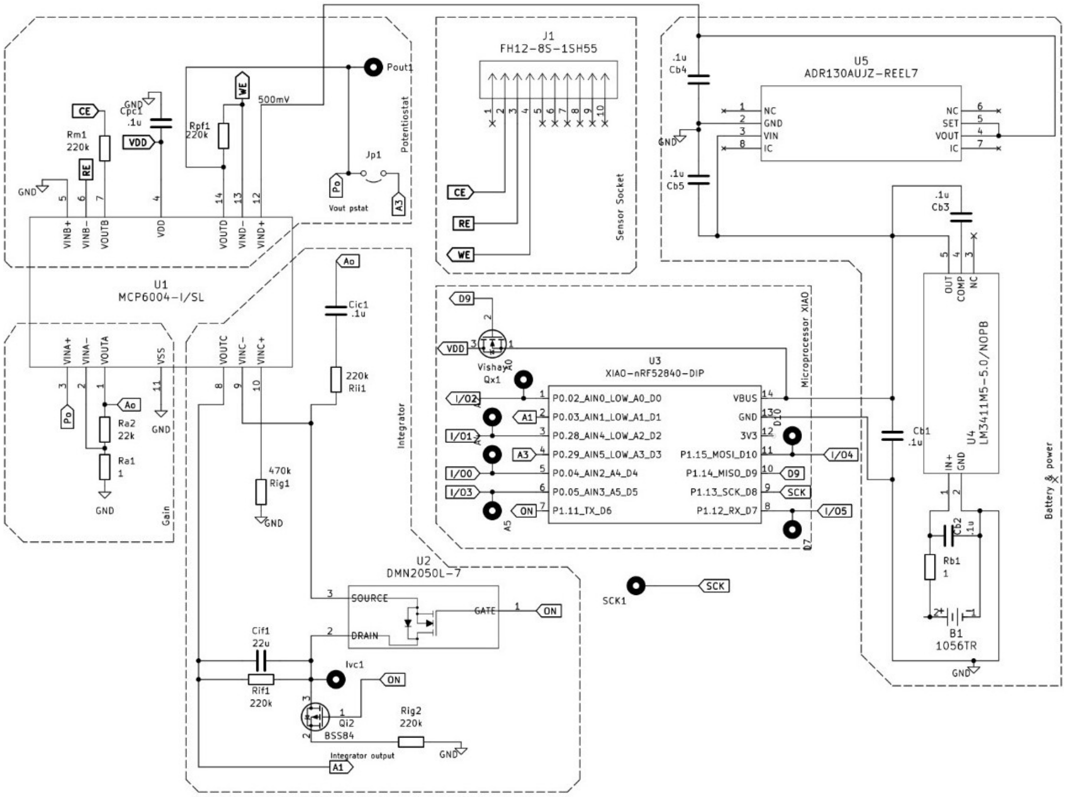

Figure 6.1: Schematic of the circuit made with KiCad 9.0.

6.2 Hand-solder Prototype

In order to realize the schematic given above in section 6.1 hand-soldered prototypes were assembled for different proposed circuits in order to asses their functioning. Notably, the integrator was made separately first to test the architecture. The integrator prototype can be seen in Figure 6.2A. The prototype of the complete schematic, as seen in the aforementioned section, can be seen in Figure 6.2B.

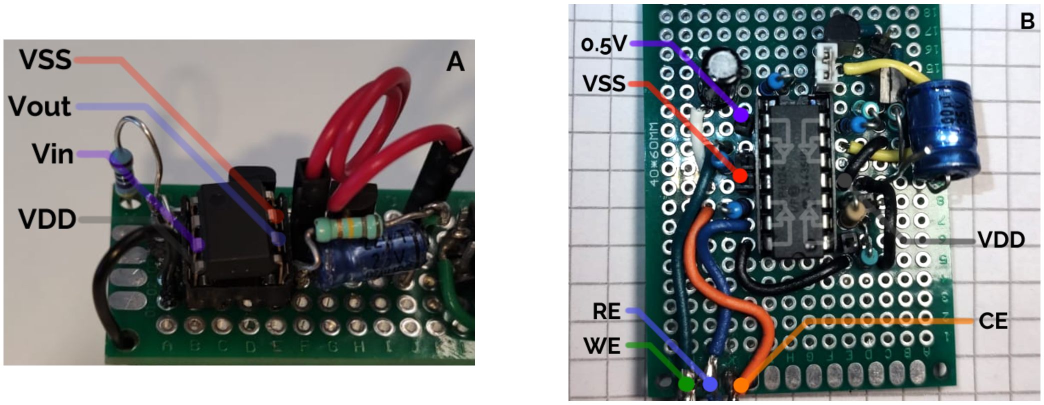

Figure 6.2: Hand-soldered prototypes of the circuits. A) Hand-soldered prototype of integrator with on/off switching architecture implemented with an OPA340 IC and transistors. B) Complete hand-soldered circuit prototype implemented with MCP6024.

The implementation was achieved with the correct values on a through-hole test board featuring an MCP2024 quad amplifier and standard E12 series components.

6.2.1 Testing

The integrator prototype (i.e., both the separate version with the OPA340 and the integrated version with the MCP2024) behaved as expected when tested using an integration window and a constant DC input to the integrator, starting 50 ms after the onset of the switching signal. A graph of the measurements can be seen in Figure 6.3.

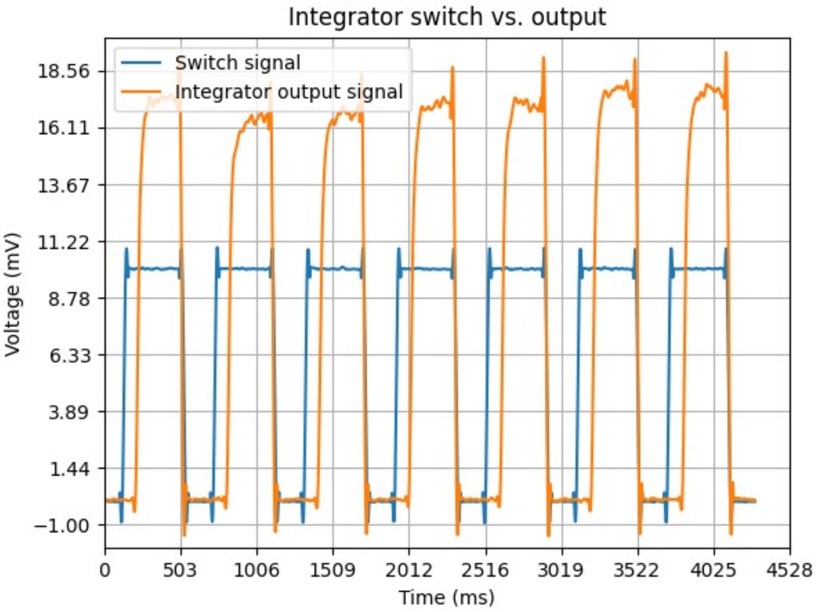

Figure 6.3: Graph of the integrator on/off switching signal plotted against the output signal with a DC input signal starting 50ms after the onset of the switching signal.

The complete prototype exhibited correct behaviours (i.e., continuity and 500 mV over the electrodes) when tested using an electrode submerged in non-distilled water.

6.3 Printed Circuit Prototype

Finally, the design was realized as a PCB using KiCad 9.0. The specifications and restrictions, as well as results from testing, will be discussed hereafter.

6.3.1 Design

For the PCB, there were certain restrictions. The decision was made to go with relatively broad leads and islands such that due to limitations of the manufacturer capabilities. Furthermore, it would be possible to further minimize the size of the PCB design. However, it was possible to keep the design within the specified size using 0603 (approximately 0.6 mm x 0.3 mm) size components. Thus, these were used. In Figure 6.4, both sides of the design can be viewed.

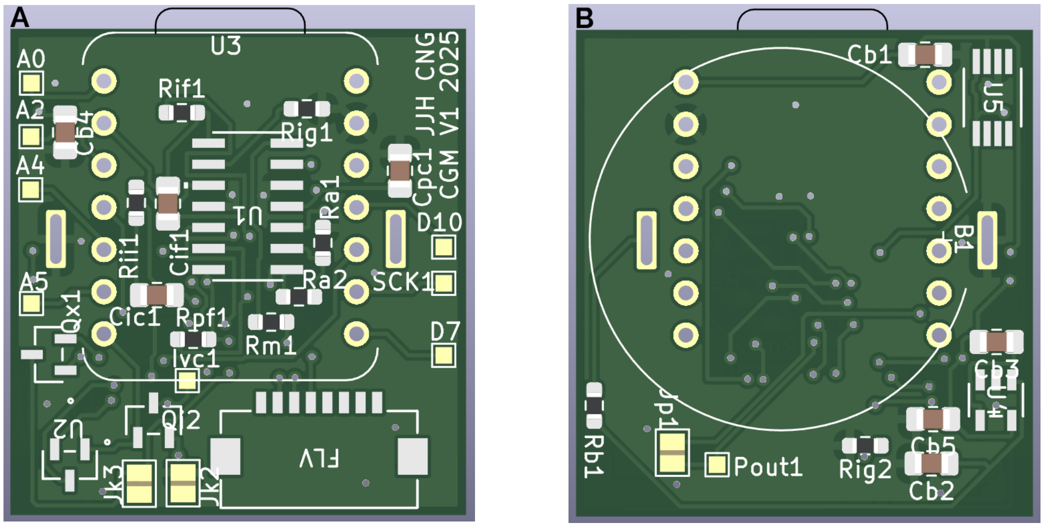

Figure 6.4: Front and backside of PCB in KiCad 9.0 software. A) Front side. B) Mirrored view of the back side.

This design was then ordered and assembled with the passive components and integrated circuits. The rationale behind these integrated circuits can be found in the paragraphs hereafter.

The **MCP6004 (U1)** is a quad amplifier IC. It was chosen for having a low bias current, such that it does not induce error in the output and drifts less over time. Moreover, the MCP6004 has a high slew rate, which allows it to respond quickly and accurately to changing signals. Finally, it was advantageous to have one IC for each of the four amplifiers required for the design. [30]

The **DMN2050L (U2, Qx1)** is an N-channel enhancement mode MOSFET. It is suited for this implementation due to having appropriate on- and off-resistance. Meaning, when it is turned on, the resistance is very small (e.g., 20-50 mΩ), and when it is turned off, the leakage is very small (e.g., nano amperes) **diodes_dmn2050**

The **Xiao nRF52840 (U3)** is the microcontroller. It was chosen for having a small surface area and built-in low-power Bluetooth capabilities. The microcontroller is suspended over the circuit in the design, such that it does not increase the area of the PCB by much. Further rationale can be found in chapter 4. [20]

The **LM3411M5 (U4)** is a 5-volt shunt regulator. This was necessary to regulate the total 6 volts provided by the batteries to a more useful 5 volts. That is, the other ICs in the design require a source voltage ranging from 3.3 to 5 volts. Furthermore, the LM3411M5 specifically is a low-power regulator, which is necessary for the PCB to make it through a 2-week use cycle. [18]

The **ADR130AUJZ (U5)** is a high-precision 500 mV reference. This reference is necessary to set the forward voltage on the electrochemical cell as described in chapter 5.1. It was chosen for its precision; the more exact the forward voltage is applied, the more accurately we can characterize the behaviour of the cell and therefore estimate the concentration of glucose in the ISF. [31]

The **BSS84 (Qi2)** is a P-channel enhancement mode field-effect transistor chosen for its low on-resistance and reliable and fast performance. [32]

Finally, in Figure 6.5, the physical PCB is seen in reference to the size of a 20-cent coin.

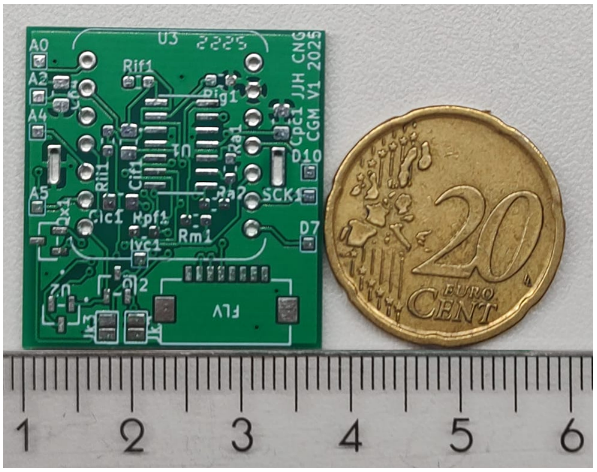

Figure 6.5: PCB as compared to a 20 cent size reference.

From this figure, it can be seen that the final dimensions of the entire PCB are approximately 27 mm x 29 mm. Specifically, the achieved surface area is 791.2mm^2.

6.3.2 Sensor

For testing with the printed circuit board, a sensor with gold electrodes was produced with similar scales to the Ribet et al. sensor. This sensor is shown in Fig, 6.6

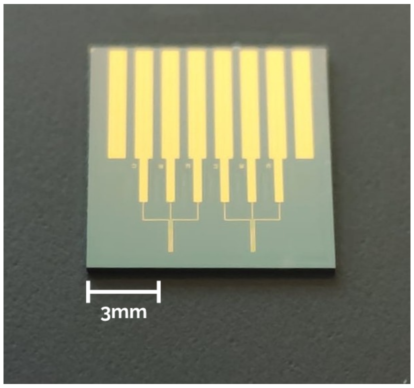

Figure 6.6: Testing electrode array made of gold.

6.3.3 Communication Protocol

In this subsection, the control protocol on the microcontroller for the PCB is explained.

Every 10 minutes, a measurement is made, and each measurement takes 23 seconds. During the measurement, the sensor is turned on, and after 2 seconds, the charge integrator is turned on. The integration window is 20 seconds, after which the value at the output of the integrator is taken as measurement, and the integrator is turned off. After one more second, the sensor is turned off.

The 10-minute loop is repeated until the sensor is replaced after two weeks, at which point the loop is started again.

6.3.4 Testing

Each stage was tested separately to ascertain the validity of these components independently. It was confirmed that the voltage regulators were functioning correctly and supplying the correct voltages.

Procedure Measurement Loop

```
Repeat ad infinitum
    SensorOn();
    Wait(2s);
    IntegratorOn();
    Wait(20s);
    Measurement();
    IntegratorOff();
    Wait(1s);
    SensorOff();
    WriteData();
    Wait(9min 37s);
```

Furthermore, the connections were tested with a multimeter to ensure connectivity wherever applicable. Then, the potentiostat was verified to enforce the correct 500 mV potential difference on the WE-RE electrodes when connected to an electrochemical cell.

The integrator was tested using a function generator. An exponentially decaying curve was applied (i.e., the reciprocal of the square root of time) at the integrator input. Thus, the expected output would be proportional to the square root of time (i.e., a rounded saw-tooth waveform). This behaviour can be seen in Figure 6.7.

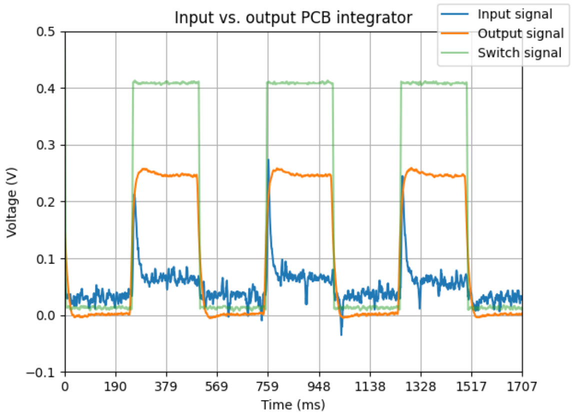

Figure 6.7: In- and output of the integrator when switched on and off.

However, despite the signals having the correct shape, the output signal on the integrator was observed to saturate too quickly.

The functioning of the entire system was tested using three gold electrodes in phosphate-buffered saline (PBS) with varying amounts of dopamine and rhodamine, with a forward voltage of 500 mV. The results for this are seen in Table 6.1.

Concentration	**Value**	**Voltage [V]**
PBS with sensor off	509	0.15V
600 mg/dl Dopamine in PBS	1456	0.42V
PBS normal measurement	1452	0.42V
300 mg/dl Dopamine in PBS	1455	0.42V

Table 6.1: Voltages at the output of the ADC as measured (in chronological order) for various concentrations of dopamine and rhodamine in PBS.

These results are congruent with the results of the saturation seen in the integrator behaviour.

7 Conclusion

7.1 Objectives

In Section 1.1 and 1.2, the purpose and objectives of this project are summarized. The primary objectives that were set are

- Bluetooth functionality,
- Separated sensor and electronics,
- Miniaturized electronics,
- Analogue Filtering, and
- Minimize noise.

The quality with which these goals were achieved can be assessed with reference to the reduction of risks posed to users as described in section 2.1.

1. Reduce cost,
2. Minimize the invasiveness and discomfort, and
3. Improve reliability

Most of these goals were achieved in a significant way.

Firstly, a Bluetooth connection was achieved in testing. Furthermore, a Bluetooth testing protocol was implemented successfully, allowing control of different parts of the circuit (i.e., turning on and off the potentiostat and integrator circuits) and transmitting the output of the ADC channels of the microcontroller to a wirelessly connected device.

Secondly, the PCB realization successfully implemented a separation of sensor and electronics. If the electrodes were to become bio-fouled, they could be replaced without having to replace the electronics. This allows for patients to replace only what must be replaced and therefore reduces the cost of care. Moreover, this feature can make using the product easier for users, as they can become more familiar with their personal electronics than when these electronics are replaced continuously.

Thirdly, the size of the prototype was well within the requirement set in Chapter 3. The surface area of the PCB was 791.1 mm^2, which is 808.9 mm^2 less than the maximally specified 1600 mm^2. When the product moves out of its prototyping phase, this size could plausibly be reduced further.

Fourthly, the analogue filtering was proven to work mathematically in Appendix C and B. However, the integrator saturated too quickly when tested with the oscilloscope and function generator. When tested with the measurement protocol, the observed value was either 0V or 1.2V at the output.

Lastly, in Section 5.3.5 the noise was found to fall within the specified range of 2.5% error.

7.2 Program of Requirements

In addition to the objectives given in Section 1.1 and 1.2. A program of requirements consisting of technical and functional requirements was also outlined in Chapter 3.

Throughout this project, the decision-making was guided by satisfying these requirements. In this section, conclusions will be drawn with reference to the requirements. The program can be seen again in Table 7.1.

Functional	Technical
- Realizable in a relatively short time frame	- Deliver 500mV to electrochemical cell
- Minimal added error	- Deliver 5V to bluetooth module
- Read out the sensor	- PCB maximum size of 40mm diameter
- Perform analogue filtering	- Less than 2.5% (±7.5mg/dl) added error
- Transmit current value over Bluetooth	- Battery functional life-time of $\geq$2 weeks
- Rechargeable	- Wireless communication over $0 - 20$ meters
- Measure every one out of ten minutes	
- Store concentration values temporarily	

Table 7.1: Program of Requirements.

7.2.1 Functional

The functional requirements prescribe what the system must be capable of to achieve the objectives. These are analysed in Table 7.2.

Functional	Conclusions
Realizable in a relatively short time frame	The implementation was realized within the time constraints of this project. Due to this, the scope of the project was limited accordingly.
Minimal added error	The added error was considered throughout the design. Resulting in a fairly limited added error. (Section 5.3.5)
Read out the sensor	In testing, it was possible to transmit some value from the ADC wirelessly to a connected device. However, a verifiable concentration measurement was not made. (Section 6.3.4)
Perform analogue filtering	Analogue filtering was performed on the signal from the potentiostat. The signal was amplified and integrated. However, the integrator saturated too quickly. (Section 6.3.4)
Transmit current value over Bluetooth	The measurements were successfully transmitted wirelessly from one device to another in the final test. (Section 6.3.4)
Rechargeable	For testing, dual CR2032 coin batteries were used. The CR2032 is not rechargeable. However, the LIR2050 of the same size is rechargeable and fits the capacity requirements. Thus, this goal was achieved. (Section 4.2) [33]
Measure every one out of ten minutes	Similarly, given the capacity of the batteries is sufficient, measuring once every ten minutes for two weeks is reached. (Section 4.2)
Store concentration values temporarily	In testing, the microcontroller was able to save values and transmit values wirelessly to connected devices. The microprocessor has sufficient memory to save a large amount of measurements when necessary. (Section 4.1)

Table 7.2: Conclusions for the program of functional requirements.

Overall, most of the functional requirements set for the system were achieved. The circuit was realized with a minimal error, analogue filtering, Bluetooth capability, recharge-ability, and storage. However, it is important to note that it has not been achieved yet to read out the sensor. This will be discussed further in Section 7.3.

7.2.2 Technical

The technical requirements give quantitative specifications for the system to adhere to. These are analysed in Table 7.3.

Each of the technical requirements was met. Most notably the $500mV$ forward voltage and the

Technical	**Conclusions**
Deliver 500mV to electrochemical cell	In testing, approximately the correct 500 mV potential difference was measured over the RE-WE electrodes. It was mathematically established that this voltage stabilized within 1 ms. (Sections A.3 and 6.3.4)
Deliver 5V to the bluetooth module	The microcontroller was powered by a 5V shunt voltage regulator. This satisfied the power and size requirements. Thus, this was achieved successfully. (Section 4.2.2)
PCB maximum size of 40mm diameter	The surface area of a 40mm diameter circle would be 1256.64mm^2. The achieved surface area was smaller than this and therefore this requirement was achieved. (Section 6.3.1)
Less than 2.5% (±7.5mg/dl) added error	The total noise contributions of the different components were summarized. The total noise specified a minimal RMS signal current of 8.36[nA] (Section 5.3.5)
Battery functional lifetime of 2 weeks	The maximal calculated lifetime based on the power usage was greater than three weeks, thus this was achieved with a large margin. (Section 4.2)
Wireless communication over 0 20 meters	The decision was made to transmit at 4.8mA current consumption. For this consumption the power requirements are satisfied and the range is up to 20 meters in optimal circumstances. Thus this requirement is generally satisfied. (Section 4.3)

Table 7.3: Conclusions for the program of technical requirements.

PCB size are crucial results. The error requirement could be investigated further, as ordering of the stages and additional filtering could further improve on this figure.

7.3 Discussion

The results of this design were satisfactory in many ways; however, it was not able to test the system from cell to output successfully. The value measured at the ADC for different concentrations was inconclusive. The observed value in testing with the function generator and in vitro indicated that the integrator and ADC saturated too soon. This indicates an oversensitivity in the system.

Assuming validity of the in vitro test, this could be solved in circuitry by decreasing the gain of the system. In the implemented design, the gain would be so great that a current larger than that which would be expected from the Ribet et al. sensor would most likely saturate the operational amplifier before reaching the input of the integrator. Moreover, the time-constant τ could be adjusted to decrease the speed at which charging and discharging happen in the integrator. Lastly, it is possible the initial assumption of an input current of $100nA$ is wrong, as it is based on very limited information. In this way the sensitivity of the system could be improved internally.

Another factor that may be improved is the AC-couple between the trans-impedance amplifier and the gain-stage. It may either be not sufficiently filtering the DC bias from the potentiostat architecture, or be filtering the Cottrell current (this is plausible, as it is low-frequency). The latter would also explain the results achieved during the full system test. Though simulation showed good filtering with $0.1\mu F$, better results may be achieved with a different value.

However, it is important to note that not all testing circumstances were ideal. A golden reference electrode cannot sustain a stable forward voltage (due to its high propensity for surface oxidation and adsorption). This might cause drift and noise at the input of the system. Moreover, using PBS as solvent might not ideally reflect behaviour in the ISF as PBS could have a higher impedance and could skew the forward voltage. These conditions can easily affect the circuit to show the behaviour seen in tests. If the circuit receives a current too large by a factor three, the integrator would already fully saturate its range. It would be prudent to test whether this is the issue by, as discussed before, reducing the different gains throughout the circuit.

7.4 Future Works

In future works, several things might be of interest when continuing this design.

1. Developing an ASIC-based implementation to reduce power consumption and further miniaturize the electronics.
2. Reducing the physical footprint of the device to improve comfort and wearability;
3. Optimizing the gain structure of the analogue front-end to better match the sensor's dynamic range.
4. Implementing an analogue Kalman filter to improve signal quality and enable real-time predictive filtering.
5. Use a step-down voltage converter instead of a shunt voltage converter, as it will likely be more efficient.
6. Test this topology with different combinations of solutions and electrodes.

Specifically, implementing the circuit as an ASIC might be highly interesting course for future works. In this way the electronics for the sensor could be reduced in size to be barely noticeable for the user and therefore more comfortable and less obstructive.

Moreover, the implementation of a Kalman filter could be highly interesting as it could simultaneously filter the signal and predict the value of the signal in the future. In this way the latency between a measurement and the value of the concentration could be reduced leading to a better user experience.

References

[1] H. King, M. Rewers, and Who Ad Hoc Diabetes Reporting Group, "Global estimates for prevalence of diabetes mellitus and impaired glucose tolerance in adults," *Diabetes Care*, vol. 16, no. 1, pp. 157–177, Jan. 1993.

[2] A. Zafar, M. Davies, A. Azhar, and K. Khunti, "Clinical inertia in management of t2dm," *Primary Care Diabetes*, vol. 4, no. 4, pp. 203–207, 2010, ISSN: 1751-9918. DOI: `https://doi.org/10.1016/j.pcd.2010.07.003`. [Online]. Available: `https://www.sciencedirect.com/science/article/pii/S1751991810000938`.

[3] J. Shaw, R. Sicree, and P. Zimmet, "Global estimates of the prevalence of diabetes for 2010 and 2030," *Diabetes Research and Clinical Practice*, vol. 87, no. 1, pp. 4–14, 2010. DOI: `https://doi.org/10.1016/j.diabres.2009.10.007`. [Online]. Available: `https://www.sciencedirect.com/science/article/pii/S016882270900432X`.

[4] Nov. 2024. [Online]. Available: `https://www.who.int/news-room/fact-sheets/detail/diabetes`.

[5] N. D. Thompson and J. F. Perz, "Eliminating the blood: Ongoing outbreaks of hepatitis b virus infection and the need for innovative glucose monitoring technologies," *Journal of Diabetes Science and Technology*, vol. 3, no. 2, pp. 283–288, 2009. DOI: `10.1177/193229680900300208`. [Online]. Available: `https://doi.org/10.1177/193229680900300208`.

[6] J. Ahn, Y. Yang, and G. Park, "Advancing elderly diabetes care: Exploring the usability and acceptance of continuous glucose monitoring (cgm)," *Geriatric Nursing*, vol. 59, pp. 15–25, 2024, ISSN: 0197-4572. DOI: `https://doi.org/10.1016/j.gerinurse.2024.06.041`. [Online]. Available: `https://www.sciencedirect.com/science/article/pii/S019745722400185X`.

[7] C. Moonla, M. Reynoso, A.-Y. Chang, T. Saha, S. Surace, and J. Wang, "Microneedle-based multiplexed monitoring of diabetes biomarkers: Capabilities beyond glucose toward closed-loop theranostic systems," *ACS Sensors*, Jun. 2025, ISSN: 2379-3694. DOI: `10.1021/acssensors.5c00652`. [Online]. Available: `http://dx.doi.org/10.1021/acssensors.5c00652`.

[8] H. Bauhaus, P. Erdogan, H. Braun, and M. Thevis, "Continuous glucose monitoring (cgm) in sports—a comparison between a cgm device and lab-based glucose analyser under resting and exercising conditions in athletes," *International Journal of Environmental Research and Public Health*, vol. 20, no. 15, 2023. DOI: `10.3390/ijerph20156440`. [Online]. Available: `https://www.mdpi.com/1660-4601/20/15/6440`.

[9] R. Holzer, W. Bloch, and C. Brinkmann, "Continuous glucose monitoring in healthy adults—possible applications in health care, wellness, and sports," *Sensors*, vol. 22, no. 5, 2022, ISSN: 1424-8220. DOI: `10.3390/s22052030`. [Online]. Available: `https://www.mdpi.com/1424-8220/22/5/2030`.

[10] F. Ribet, "Integrated microsystems for continuous glucose monitoring, interstitial fluid sampling and digital microfluidics," Ph.D. dissertation, KTH, Micro and Nanosystems, 2020.

[11] E. Kalyva, E. Malakonaki, C. Eiser, and D. Mamoulakis, "Health-related quality of life (hrqol) of children with type 1 diabetes mellitus (t1dm): Self and parental perceptions," *Pediatric Diabetes*, vol. 12, no. 1, pp. 34–40, Jan. 2011, ISSN: 1399-543X. DOI: `10.1111/j.1399-5448.2010.00653.x`. [Online]. Available: `http://dx.doi.org/10.1111/j.1399-5448.2010.00653.x`.

[12] A. Nieuwesteeg, F. Pouwer, R. van der Kamp, H. van Bakel, H.-J. Aanstoot, and E. Hartman, "Quality of life of children with type 1 diabetes: A systematic review," *Current Diabetes Reviews*, vol. 8, no. 6, pp. 434–443, Oct. 2012, ISSN: 1573-3998. DOI: `10.2174/157339912803529850`. [Online]. Available: `http://dx.doi.org/10.2174/157339912803529850`.

[13] T. Shi, D. Li, G. Li, Y. Zhang, K. Xu, and L. Lu, "Modeling and measurement of correlation between blood and interstitial glucose changes," *Journal of Diabetes Research*, vol. 2016, pp. 1–9, 2016, ISSN: 2314-6753. DOI: `10.1155/2016/4596316`. [Online]. Available: `http://dx.doi.org/10.1155/2016/4596316`.

[14] C. Erkmen, D. N. Unal, S. Kurbanoglu, and B. Uslu, "Basics of electrochemical sensors," in *Organic Electrodes: Fundamental to Advanced Emerging Applications*, R. K. Gupta, Ed. Cham: Springer International Publishing, 2022, pp. 81–99, ISBN: 978-3-030-98021-4. DOI: `10.1007/978-3-030-98021-4_5`. [Online]. Available: `https://doi.org/10.1007/978-3-030-98021-4_5`.

[15] S. Vesztergom, "A short introduction to digital simulations in electrochemistry: Simulating the cottrell experiment in ni labview," *Journal of Electrochemical Science and Engineering*, vol. 8, no. 2, pp. 171–181, May 2018, ISSN: 1847-9286. DOI: `10.5599/jese.507`. [Online]. Available: `http://dx.doi.org/10.5599/jese.507`.

[16] N. Jendrike, A. Baumstark, U. Kamecke, C. Haug, and G. Freckmann, "ISO 15197: 2013 evaluation of a blood glucose monitoring system's measurement accuracy," en, *J. Diabetes Sci. Technol.*, vol. 11, no. 6, pp. 1275–1276, Nov. 2017.

[17] F. Ribet, G. Stemme, and N. Roxhed, "Ultra-miniaturization of a planar amperometric sensor targeting continuous intradermal glucose monitoring," en, *Biosens. Bioelectron.*, vol. 90, pp. 577–583, Apr. 2017.

[18] Texas Instruments, *Lm3411 precision secondary regulator and driver*, `https://www.ti.com/product/LM3411`, Rev. F, May 2016. [Online]. Available: `https://www.ti.com/product/LM3411`.

[19] C. Gomez, J. Oller, and J. Paradells, "Overview and evaluation of bluetooth low energy: An emerging low-power wireless technology," *Sensors*, vol. 12, no. 9, pp. 11 734–11 753, 2012, ISSN: 1424-8220. DOI: `10.3390/s120911734`. [Online]. Available: `https://www.mdpi.com/1424-8220/12/9/11734`.

[20] *Getting Started with Seeed Studio XIAO nRF52840 Series | Seeed Studio Wiki — wiki.seeedstudio.com*, `https://wiki.seeedstudio.com/XIAO_BLE/`, [Accessed 05-05-2025].

[21] F. Ribet, G. Stemme, and N. Roxhed, "Real-time intradermal continuous glucose monitoring using a minimally invasive microneedle-based system," en, *Biomed. Microdevices*, vol. 20, no. 4, p. 101, Dec. 2018.

[22] Š. Komorsky-Lovrić, "Working electrodes," in *Electroanalytical Methods: Guide to Experiments and Applications*, F. Scholz, A. M. Bond, R. G. Compton, *et al.*, Eds., Berlin, Heidelberg: Springer Berlin Heidelberg, 2010, pp. 273–290.

[23] M. Bogdan, D. Brugger, W. Rosenstiel, and B. Speiser, "Estimation of diffusion coefficients from voltammetric signals by support vector and gaussian process regression," *Journal of cheminformatics*, vol. 6, p. 30, May 2014. DOI: `10.1186/1758-2946-6-30`.

[24] A. J. Bard and L. R. Faulkner, *Electrochemical methods and applications.* Wiley-Interscience, 2000.

[25] M. M. Ahmadi and G. A. Jullien, "Current-mirror-based potentiostats for three-electrode amperometric electrochemical sensors," *IEEE Transactions on Circuits and Systems I: Regular Papers*, vol. 56, no. 7, pp. 1339–1348, 2009. DOI: `10.1109/TCSI.2008.2005927`.

[26] X. Yang, J. Yang, L.-f. Lin, and C.-d. Ling, "Low-power low-noise cmos chopper amplifier," in *2010 International Conference on Anti-Counterfeiting, Security and Identification*, 2010, pp. 83–84. DOI: `10.1109/ICASID.2010.5551831`.

[27] M. A. Akram, A. Aberra, S.-J. Kweon, and S. Ha, "An ultra-low-power amplifier-less potentiostat design based on digital regulation loop," *IEEE Transactions on Biomedical Circuits and Systems*, pp. 1–12, 2025. DOI: `10.1109/TBCAS.2025.3527652`.

[28] R. E. Kalman, "A new approach to linear filtering and prediction problems," en, *J. Basic Eng.*, vol. 82, no. 1, pp. 35–45, Mar. 1960.

[29] D. van de Pol and B. R. Menkveld, "Digital glucose modelling," TU Delft, 2025.

[30] Microchip Technology Inc., *Mcp6004: Quad 1.8v, 600na op amps with rail-to-rail input and output*, Datasheet DS20001733L, 2016. [Online]. Available: `https://www.microchip.com/en-us/product/MCP6004`.

[31] Analog Devices, *Adr130: Precision series sub-band gap voltage reference*, `https://www.analog.com/en/products/adr130.html`, Rev. D, Aug. 2018. [Online]. Available: `https://www.analog.com/en/products/adr130.html`.

[32] Diodes Incorporated, *Bss84: P-channel enhancement-mode mosfet, sot-23*, Datasheet, DS30149 Rev.26, July 2024, 2024. [Online]. Available: `https://www.diodes.com/datasheet/download/BSS84.pdf`.

[33] EEMB, *LIR2050 Rechargeable Lithium-ion Coin Cell Batteries, 3.7V 100mAh*, `https://www.amazon.com/EEMB-LIR2050-Rechargeable-Lithium-ion-Batteries/dp/B0C61PTK65?utm_source=chatgpt.com`, Accessed: 2025-06-16, 2023.

[34] EL-CELL GmbH, *Pat-dummy-cellii: Three-electrode dummy cell for potentiostat testing*, Product overview and specifications, 2025.

[35] B. Razavi, *Design of Analog CMOS Integrated Circuits*. McGraw-Hill, 2001, ISBN: 9780072380323.

A Potentiostat Circuit Analysis

In this appendix there is an analysis of the potentiostat circuit proposed in Chapter 5.1. To this end, nodal analysis is performed. Consider the circuit as it is given in Chapter 5.1.

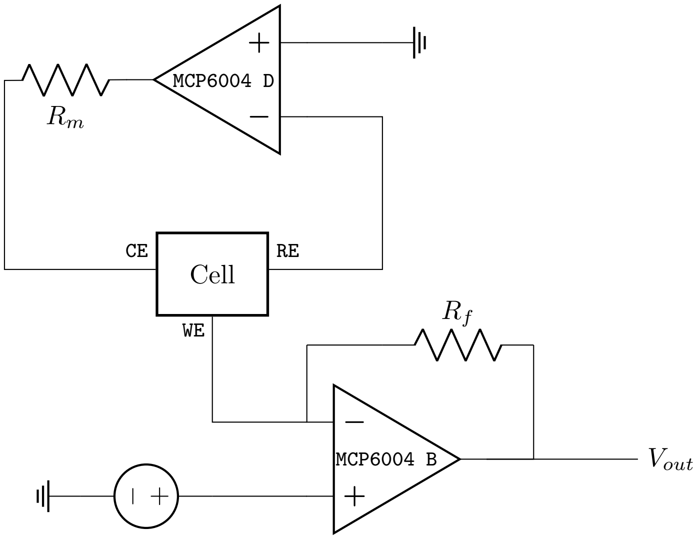

Figure A.1: Schematic for Potentiostat utilizing MCP6004 op-amp IC.

Potentiostat

It is assumed that the amplifier is ideal. Thus there flows no current into the inverting input of the amplifier. From this is it clear $I_{RE} = 0$, which by extension means $I_{CE} = I_{WE}$. This current originates from electro-chemical processes discussed in Appendix D. Quantifying this current is beyond the scope of this appendix.

Trans-Impedance Amplifier

This current then flows directly into the second amplifier. Now KCL is applied at the inverting terminal of the amplifier to quantify the output voltage.

$$-I_{WE} + \frac{V^- - V_{out}}{R_f} = 0 \tag{A.1}$$

Given that the amplifier has a sufficient open-loop gain to enforce $V^- = V^+ = V_s$. Equation (A.1) can be rewritten to Equation (A.2).

$$V_{out} = -R_f I_{WE} + V_s \tag{A.2}$$

It is important to note that the output will always contain a $500mV$ offset

A.1 Noise

First the thermal noise of the different resistors is calculated. This is done using Equation (A.3).

$$V_{n,i} = \sqrt{4kTR_i} \tag{A.3}$$

Additionally, it is assumed there is a noise coming out of the cell. This noise has numerous sources; chemical/mechanical noise, drift, etc. The noise coming from the two resistors $R_m = R_f = 22K\Omega$ is calculated as:

$$V_{n,m} = V_{n,f} = \sqrt{4kTR_m} = 60.9[\mathrm{nV}/\sqrt{\mathrm{Hz}}] \tag{A.4}$$

The noise from the cell and the resistors is not subject to any amplification. Thus, it can be said this noise is directly the input referred noise. Now the noise coming from the amplifier is considered. The data-sheet from the MCP6004 [30] specifies a input voltage density of $V_{\mathrm{amp,v}} = 28[\mathrm{nV}/\sqrt{\mathrm{Hz}}]$. Additionally, it is subject to an input noise current of $I_{\mathrm{amp}} = 0.6[\mathrm{fA}/\sqrt{\mathrm{Hz}}]$. To convert the input noise current to input noise voltage the equivalent impedance is calculated as.

$$V_{\mathrm{amp,i}} = 0.6 \times 10^{-15} \cdot 22 \times 10^3 = 13.2[\mathrm{pV}/\sqrt{\mathrm{Hz}}] \tag{A.5}$$

The total input referred noise spectral density can then be found in Equation (A.6).

$$V_n = \sqrt{V_{n,a}^2 + V_{n,b}^2 + V_{\mathrm{amp},v}^2 + V_{\mathrm{amp},i}^2} = 28[\mathrm{nV}/\sqrt{\mathrm{Hz}}] \tag{A.6}$$

Note that this equation does not account for the noise coming from the chemical cell. This noise is difficult to quantitively describe. [10] suggests Gaussian noise with 10 percent standard deviation. This is however just a suggestion. A better practice would be to measure the noise under natural wear. If the noise is taken have an RMS value 50% of the signal strength, the total input referred noise density is found as $V_{\mathrm{cell}} = 50\% \cdot 100n = 50[nV/\mathrm{Hz}]$

$$V_n = \sqrt{V_{n,a}^2 + V_{n,b}^2 + V_{\mathrm{amp},v}^2 + V_{\mathrm{amp},i}^2 + V_{\mathrm{cell}}^2} = 57.3[\mathrm{nV}/\sqrt{\mathrm{Hz}}] \tag{A.7}$$

A.2 Power

The power consumption from the operational amplifier is found via the quiescent current. In the data-sheet of the MCP6004 [30] it is found that the quiescent current is $I_Q = 100 \times 10^{-6}$. The power consumed by the op-amp is therefore found in Equation (A.8).

$$P_{\mathrm{amp}} = 2 \cdot V_{\mathrm{supply}} \cdot I_Q = 2 \cdot 5 \cdot 100 \times 10^{-6} = 1[mW] \tag{A.8}$$

There also power consumption by the resistors, however the power consumption coming from the $R_f = 22k\Omega$ resistor is neglected as assuming an $100nA$ input current yields a power consumption in the pW ranges.

A.3 Simulation

Simulation for the full potentiostat topology is challenging as LtSpice has no reliable method of simulating an electrochemical cell. For the purposes of simulation a Randles model is applied. The Randles model is an equivalent circuit used to represent the impedance of an electrochemical cell. It consists of a solution resistance R_s in series with a parallel combination of the double-layer capacitance C_{dl} and the charge transfer resistance R_{ct}. Optionally, a Warburg impedance Z_W can be included in parallel to model the electrochemical behaviour (namely, the Cottrell equation). Since the inclusion of the Warburg impedance is beyond the scope of the project it is also omitted from the LtSpice circuit. The values chosen for the simulation are chosen to represent an optional "Dummy Cell" that is available to test the circuit. The DummyCell2 is [34] available to the project. A schematic overview of the cell is shown Figure A.2

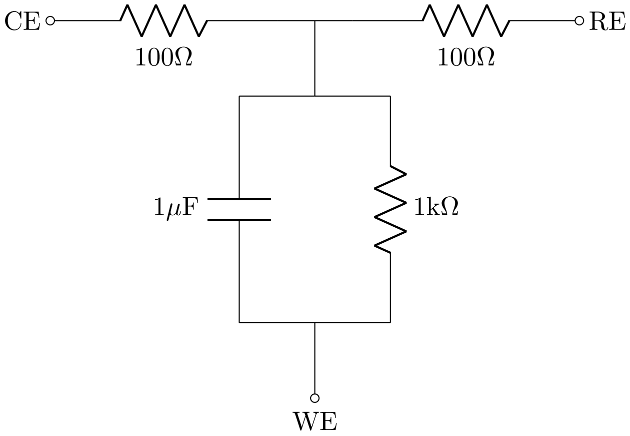

Figure A.2: Randles model equivalent circuit

A circuit to simulate the potentiostat is created according to Figures A.1 and A.2. Additionally, the amplifiers were DC coupled using a $0.1\mu F$ capacitor. This circuit is simulated until steady-state is achieved. Figure A.3 shows initial oscillation occurring in the $500mV$ voltage between the working and reference electrode. The trans-impedance amplifier shows the expected amplification of the ingoing current. This graph is excluded from this appendix. As the omission of the Warburg impedance means this current is not representative of the potentiostat output voltage with an genuine chemical cell connected. Figure A.3 shows oscillations of the control voltage $V_{WE} - V_{WE}$. It is important to have the circuit settle before opening the integration window.

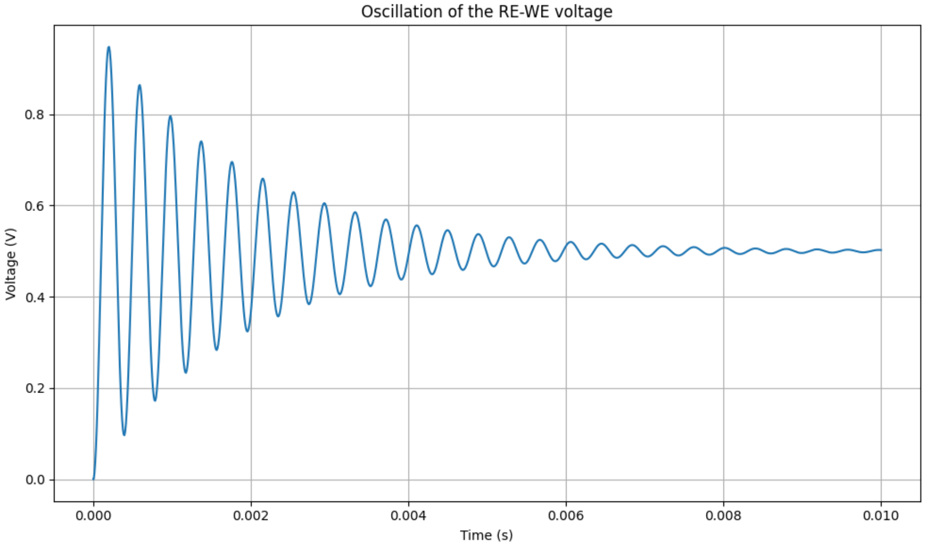

Figure A.3: Graph of the simulated wE-RE voltage

B Gain Stage Circuit Analysis

B.1 Transfer Function

In this appendix the gain stage proposed in Section 5.2 is analysed. The circuit is shown in image B.1. Nodal analysis is performed on the negative feedback terminal of the op-amp. Since the circuit is configured with a feedback loop it is assumed that:

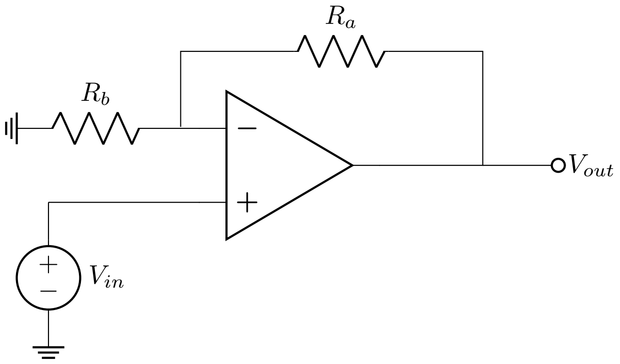

Figure B.1: Gain stage implementation

$$V^- = V^+ = V_{in} \tag{B.1}$$

Nodal analysis on the negative feedback terminal gives:

$$\frac{V_{in}}{R_b} + \frac{V_{in} - V_{out}}{R_a} = 0 \tag{B.2}$$

Equation (B.2) can be algebraically rewritten to Equation (B.3).

$$V_{out} = V_{in}\left(\frac{R_a}{R_b} + 1\right) \tag{B.3}$$

From this equation it is clear the transfer equation for the gain stage is given in Equation (B.4).

$$H(f) = \frac{R_a}{R_b} + 1 \tag{B.4}$$

B.2 Noise

The circuit has multiple noise sources. Namely, two resistors and one amplifier. The noise coming from the resistors can be calculated using Equation (B.5).

$$V_{n,i} = \sqrt{4kTR_i} \tag{B.5}$$

Using Equation (B.5) with $R_a = 22k\Omega$ and $R_b = 1\Omega$, two noise sources sources can be quanitified.

$$V_{n,a} = \sqrt{4kTR_a} = 0.13[\text{nV/Hz}]$$

$$V_{n,b} = \sqrt{4kTR_b} = 19.1[\mathrm{nV}/\sqrt{\mathrm{Hz}}]$$

The second source need to be input referred by using the gain calculated in Equation (B.4). Therefore the input-referred thermal noise coming from R_b can be found in Equation (B.6).

$$V_{n,b} = \frac{19.1 \times 10^{-9}}{22001} = 0.87[\mathrm{pV}/\sqrt{\mathrm{Hz}}] \tag{B.6}$$

Now, the noise coming from the amplifier is considered. The data sheet from the MCP6004 [30] specifies a input voltage density of $V_{\mathrm{amp,v}} = 28[\mathrm{nV}/\sqrt{\mathrm{Hz}}]$. Additionally, it is subject to an input noise current of $I_{\mathrm{amp}} = 0.6[\mathrm{fA}/\sqrt{\mathrm{Hz}}]$. The total spectral noise density is found in Equation (B.7).

$$V_n = \sqrt{V_{n,a}^2 + V_{n,b}^2 + V_{\mathrm{amp},v}^2 + V_{\mathrm{amp},i}^2} = 28[\mathrm{nV}/\sqrt{\mathrm{Hz}}] \tag{B.7}$$

B.3 Power

In this section the total power consumed by thisstage is calculated Equation (B.8).

$$P_{\mathrm{amp}} = V_{\mathrm{supply}} \cdot I_Q = 5 \cdot 100 \times 10^{-6} = 0.5[mW] \tag{B.8}$$

The feed-back resistor will have a voltage related to the output of the trans-impedance amplifier. This power consumption will also be negligible due to the large value of the R_b resistor. The result will be in the μW range.

B.4 Simulation

LtSpice simulations were created for this circuit under the conditions proposed in Chapter 5.2. Namely, $R_a = 22K\Omega$ and $R_b = 1\Omega$. A linear voltage sweep ranging from 0V to 2V was performed on the circuit shown in Figure B.1. A generic amplifier model native to LtSpice was used with values lifted from the MCP6004 datasheet. Most importantly, an open loop gain of $A_{vol} = 400K$. The simulation performed as expected, showing a $H(f) \approx 20K$ amplification. It is believed the gain is lower in the model with respect to Equation (5.6) due to finite open-loop gain. The actual open-loop gain can be found using Equation (B.9).

$$H'(f) = \frac{A_{vol}}{1 + A_{vol}/H(f)} \tag{B.9}$$

Entering $A_{vol} = 400K$ and $H(f) = 20K$ it is found that:

$$H'(f) = \frac{400 \times 10^3}{1 + 400 \times 10^3/22 \times 10^3} = 20.9K \tag{B.10}$$

C Integrator Circuit Analysis

In this appendix, circuit analysis will be performed on the integrator circuit discussed in Section 5.2.2. For the analysis an equivalent model will be used for the NMOS and PMOS transistor. The integrator topology with the equivalent transistor models is shown in Images C.1 and C.2.

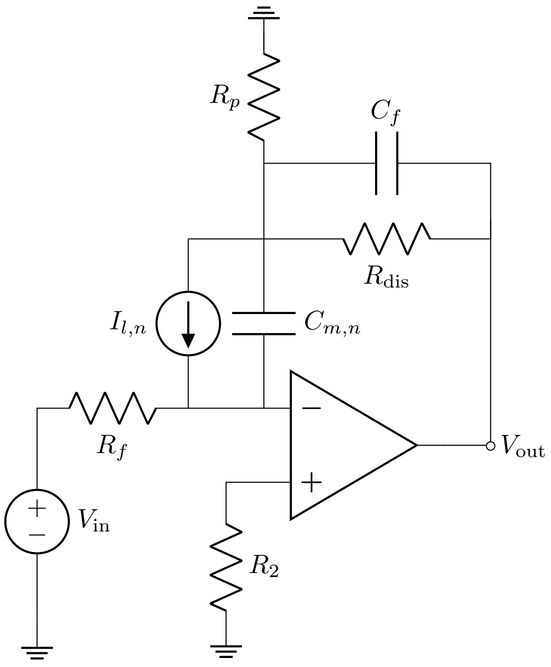

Figure C.1: Integration Circuit: Discharge

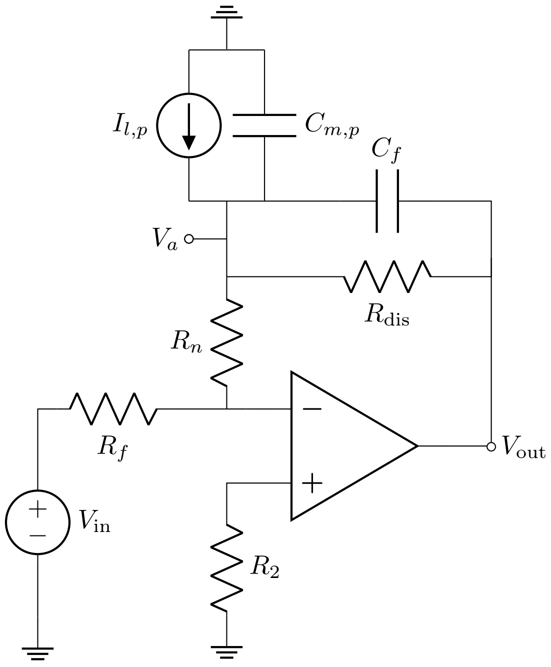

Figure C.2: Integration Circuit: Integration

C.1 Integration Mode

In this section, the circuit's integration mode is analysed. The goal of integration mode is to refer the signal from the input to the output via Equation (C.1). However due to non-idealities of the switches, the actual signal path will be different.

$$V_{out} = -\frac{1}{R_f C_f} \int V_{in} dt \tag{C.1}$$

The non-ideal expression is derived to quantify the effect of the MOSFETS on the integrating behaviour of the integrator circuit.

Node A

First, nodal analysis is done on node A. Which connects the two MOSFET switches to the output path.

$$\frac{V_a - V^-}{R_n} + \frac{V_a - V_{\text{out}}}{R_{\text{dis}}} + \frac{V_a - V_{out}}{Z_{C_f}} + \frac{V_a - \text{GRND}}{Z_{C_{m,p}}} - I_{L,p} = 0 \tag{C.2}$$

It is assumed that there is sufficient open-loop gain to enforce $V^- = V^+ = 0$. Equation (C.2) can be rewritten to find Equation (C.3).

$$V_a\left[\frac{1}{R_n}+\frac{1}{R_{\text{dis}}}+sC_f+sC_{m,p}\right]=I_{l,p}+V_{out}\left[\frac{1}{R_{\text{dis}}}+sC_f\right] \tag{C.3}$$

Inverting Terminal

Secondly, an expression for V_a is found using nodal analysis at the inverting input. The sum of currents is:

$$\frac{V^- - V_{in}}{R_f}+\frac{V^- - V_a}{R_n}=0 \tag{C.4}$$

Again, it is assumed there is sufficient open loop gain. Under that assumption Equation (C.4) becomes:

$$V_a=-\frac{R_n}{R_f}V_{in} \tag{C.5}$$

Result

Combining Equations (C.4) and (C.6) yields Equation (C.6). This expression directly relates the output voltage to the input voltage in the Laplace domain. This equation can be used to find the time-domain behaviour of integrator circuit.

$$V_{\text{out}}=\frac{(V_{\text{in}}-R_fI_{L,p})\left(s(C_{m,p}+C_f)+\dfrac{1}{R_n}+\dfrac{1}{R_{\text{dis}}}\right)}{sC_{m,p}R_f\left(sC_f+\dfrac{1}{R_{\text{dis}}}\right)} \tag{C.6}$$

To simplify the model, numerous assumptions can be made. First, $C_{m,p} \ll C_f$. The data-sheet of the DMN2050 **diodes_dmn2050** specifies a Miller capacitance of $117pF$, whilst the feedback capacitance is chosen in Section 5.2 to be $47\mu F$. Secondly, $R_n \ll R_{\text{dis}}$. They are valued 1.2Ω and $220k\Omega$ respectively.

$$V_{\text{out}}=\frac{(V_{\text{in}}-R_fI_{L,p})\left(1+\dfrac{1}{sC_{m,p}R_n}\right)}{R_f\left(sC_f+\dfrac{1}{R_{\text{dis}}}\right)} \tag{C.7}$$

This expression is evaluated using the Scipy signal library. The component values determined in Section 5.2 were used for simulation. To mimic the decay shown in the Cottrell equation, exponential decay is used as an input. The input signal was an exponential decay of the form $V_0\exp(-at)$ with $a=\{3,10,50\}$ and $V_0=2V$. The resulting plot is shown in Figure C.3.

Additionally, this result is compared to the ideal integrator discussed in Section C.1. In python both outputs were calculated for the same exponential decay signals specified for Figure C.3. The results are summarized in Table C.1.

	$a=3$	$a=10$	$a=50$
RMS Error	0.0185	0.0092	0.0022

Table C.1: RMS error between simulated V_{out} and ideal integrator output for different exponential decay rates.

From this, it can be inferred the circuit behaves similarly to the ideal integrator configuration. Therefore, the time-constant for charging is found as $\tau = C_fR_f$.

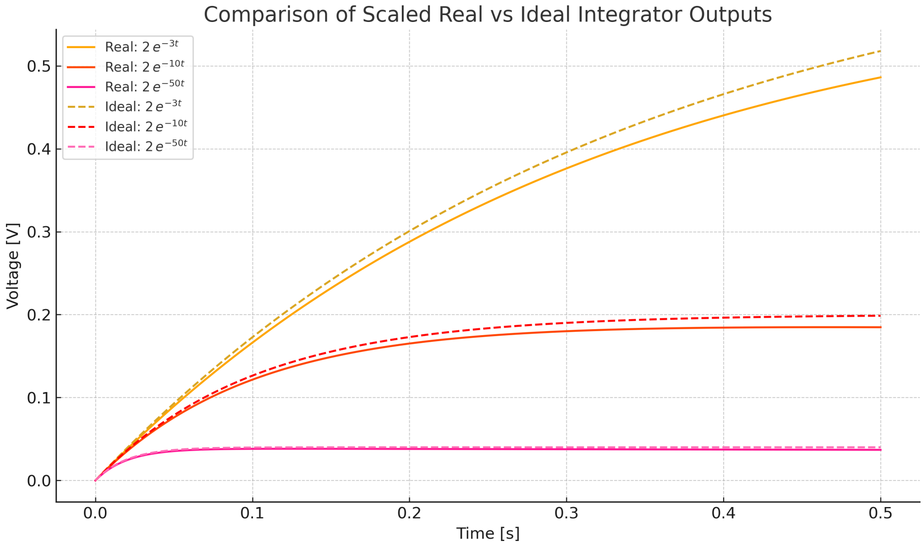

Figure C.3: The output voltage of the integrator circuit simulated with different values

C.2 Discharge Mode

After integrating over a sufficient period (as described in Section C.1). It is essential to discharge the capacitor C_f before the next integration cycle. To this end the capacitor is shorted to ground using the NMOS-PMOS switching pair. The following equations will define an expression for the output voltage during the discharge cycle along with a time-constant for discharging.

Node A

First, nodal analysis is done on node A. It connects the two MOSFETS to the integration path.

$$\frac{V_a - V^-}{Z_{Cm,n}} + \frac{V_a - V_{out}}{R_{\text{dis}}} + \frac{V_a - V_{out}}{Z_{C_f}} + \frac{V_a - \text{GRND}}{R_p} \tag{C.8}$$

Rewriting Equation (C.8) and filling in $Z_C = 1/sC$ gives Equation (C.9). Note that it is assumed in this step that $V^- = V^+$, which is only true for a sufficient open-loop gain.

$$V_{\text{out}} = \frac{s(C_{m,n} + C_f) + \frac{R_p R_{\text{dis}}}{R_p + R_{\text{dis}}}}{sC_f + \dfrac{1}{R_{\text{dis}}}} \tag{C.9}$$

Inverting Terminal

Nodal analysis is performed at the inverting terminal of the amplifier. The sum of the currents is given in Equation (C.10).

$$-\frac{V_{in}}{R_f} - \frac{V_a}{Z_{C_{m,n}}} = I_{l,n} \tag{C.10}$$

This can be rewritten to Equation (C.11).

$$V_{in} = sC_{m,n}R_f V_a + R_f I_{l,n} \tag{C.11}$$

Result

The final expression is found by substituting Equation (C.11) into Equation (C.9). Doing so gives:

$$V_{\text{out}} = \frac{(V_{\text{in}} - R_f I_{l,n}) \left(s(C_{m,n} + C_f) + \dfrac{1}{R_{\text{dis}}} + \dfrac{1}{R_p} \right)}{sC_{m,n} R_f \left(sC_f + \dfrac{1}{R_{\text{dis}}} \right)} \tag{C.12}$$

The goal is to find a corresponding time-domain expression for this equation. First, it is known that $R_{\text{dis}} = R_p = R_f = 220k\Omega$. The actual value of R_p is found as the sum of the on-resistance of the P-channel MOSFET (BSS84) [32] $R_{on} = 10\Omega$, and the series resistor $R_s = 220k\Omega$. Additionally, it is known $C_{m,n} \ll C_f$. This is because C_f is selected to be $47\mu F$ in Section 5.2 and the N-channel MOSFET Miller capacitance is specified on the data sheet of the DMN2050 **diodes_dmn2050** to be $C_{m,n} = 117pF$. Using these simplification, Equation (C.13) is found.

$$V_{\text{out}} = \frac{(V_{\text{in}} - R_f I_{l,n}) \left(sC_f + \dfrac{2}{R_f} \right)}{sC_{m,n} R_f \left(sC_f + \dfrac{1}{R_f} \right)} = \frac{(V_{\text{in}} - R_f I_{l,n}) \left(sC_f + \dfrac{2}{R_f} \right)}{sC_{m,n} R_f \left(sC_f + \dfrac{1}{R_f} \right)} \tag{C.13}$$

Using partial decomposition (C.14), can be found.

$$V_{out} = \frac{V_{in} - R_f I_{l,n}}{R_f C_{m,n}} \left(\frac{2}{s} - \frac{C_f}{sC_f + \frac{1}{R_f}} \right) \tag{C.14}$$

Note that on this time-scale the input voltage V_{in} can be though of as a DC voltage. This voltage is represented in the Laplace domain as V_0/s.

$$V_{\text{out}} = \frac{1}{C_{m,n}} \left[\frac{2V_0}{R_f s^2} - \frac{V_0 C_f}{R_f s(sC_f + a)} - \frac{2I_{l,n}}{s} + \frac{I_{l,n} C_f}{sC_f + a} \right] \tag{C.15}$$

Distributing the terms in Equation (C.15) gives:

$$V_{\text{out}}(s) = \frac{1}{C_{m,n}} \left[\frac{2V_0}{R_f s^2} - \frac{V_0 C_f}{R_f s(sC_f + a)} - \frac{2I_{l,n}}{s} + \frac{I_{l,n} C_f}{sC_f + a} \right] \tag{C.16}$$

The inverse Laplace transform for Equation (C.16) can be found as Equation (C.17).

$$V_{\text{out}}(t) = \frac{1}{C_{m,n}} \left[\frac{2V_0}{R_f} t + (V_0 R_f + I_{l,n})\, e^{-\frac{t}{R_f C_f}} - (V_0 R_f + 2I_{l,n}) \right] \tag{C.17}$$

From here it is clear that there are three basic terms; a constant DC term that leaks charge out of the capacitor via the N-channel MOSFET, a ramp term that charges the capacitors, and an exponential term that signifies an instant decay. For the initial decay the exponential is the most significant term. The time-constant is found using python simulation as $2\mu s$.

C.3 Power

There are two resistors that are consuming a measurable amount of power. Additionally, there is a single integrated circuits. The power dissipation in the integrator circuit consists singularly of the power consumed by the amplifier. As all other power consumptions are in the μW ranges. The circuit has only a single integrator, thus power consumption will be $0.5[mW]$

C.4 Noise

In this section the noise of the integrator circuit is calculated. The noise will be roughly the same regardless of what mode the circuit is in. The total noise in the system is described in Equation (C.18).

$$V_n = \sqrt{V_{R_f}^2 + V_{R_{\text{dis}}}^2 + V_{\text{NMOS}}^2 + V_{i,\text{amp}}^2 + V_{v,\text{amp}}^2} \tag{C.18}$$

The thermal noise coming from the resistors is found as $V_{R_f} = V'_{R_{\text{dis}}} = 60.4[nV/HZ]$. Note that to make the noise $V_{R_{\text{dis}}}$ input referred, it needs to be multiplied by the ideal integrator gain and also be summed over the whole bandwidth. The resulting noise will be coloured.

$$V_{R_{\text{dis}}} = V'_{R_{\text{dis}}} \cdot R_f C_f \cdot 2\pi f = 3.92f[\mu V/\sqrt{\text{Hz}}] \tag{C.19}$$

Now, the noise coming from the amplifier is considered. The data sheet from the MCP6004 specifies a input voltage density of $V_{\text{amp,v}} = 28[\text{nV}/\sqrt{\text{Hz}}]$. Additionally, it is subject to an input noise current of $I_{\text{amp}} = 0.6[\text{fA}/\sqrt{\text{Hz}}]$. Lastly, the input-referred noise coming from the N-Channel MOSFET is considered. The input referred noise of any MOSFET can be found as: [35].

$$V_{\text{NMOS}} = \sqrt{4kTR_{DS}} = 12.9[nV/\sqrt{\text{Hz}}] \tag{C.20}$$

Entering all of these noise sources into Equation (C.18), gives Equation (C.21).

$$V_n = \sqrt{V_{R_f}^2 + V_{R_{\text{dis}}}^2 + V_{\text{NMOS}}^2 + V_{i,\text{amp}}^2 + V_{v,\text{amp}}^2} = 90.7[nV/\sqrt{\text{Hz}}] \tag{C.21}$$

C.5 Simulation

In this final section an LtSpice simulation is done to test the feasibility of the proposed circuit. To this end, a component was created that implements the integrator circuit. For this circuit, the BSS84 and BSP89 were used since there was no LtSpice component was available for the DMN2050. For the control signal of the switching pair a pulse was selected with $T = 12[s]$ and $D = 0.5$. For the input signal $V_{in} = 2[V]$ was applied. The resulting graph is shown in Figure C.4.

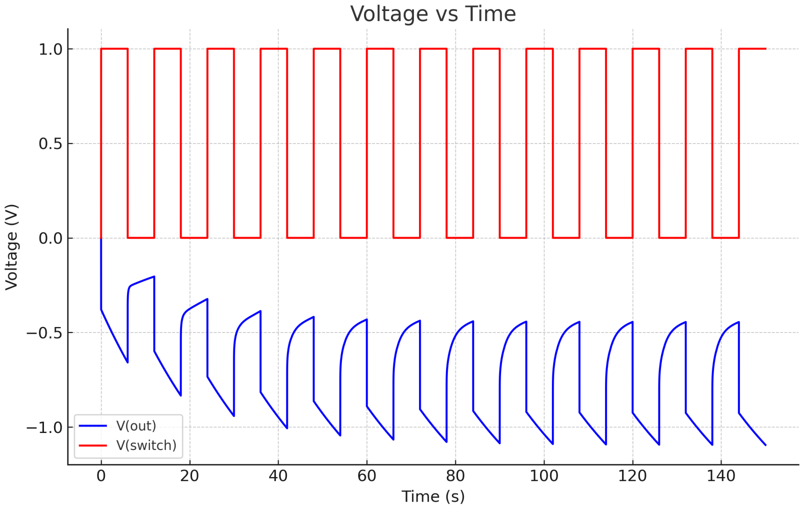

Figure C.4: The output voltage of the integrator circuit simulated with different values

D Electrode Diffusion Mechanics

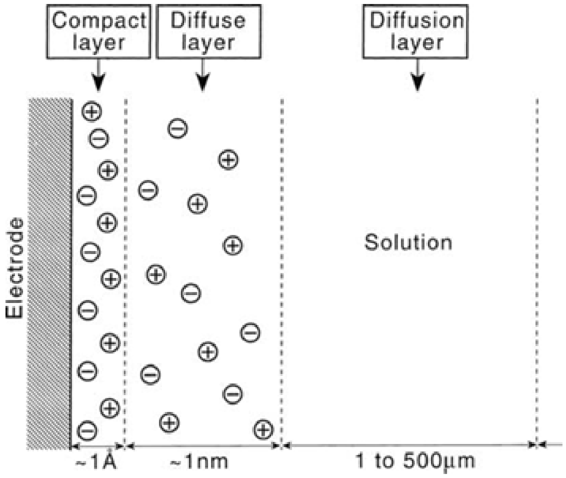

Figure D.1: Schematic representation of the composition of the solution phase in the vicinity of the electrode surface (not to scale) by Komorsky-Lovric et al [22].

The concentration of the oxidized molecule at the surface of the electrode ($[A]_{x=0}$) can be related to the concentration in the bulk of the solution ($[A]_{bulk}$) through using Fick's law and Nernst's law as seen in Equation (D.1) and Equation (D.2) respectively.

$$\frac{d[A]}{dt} = D\frac{d^2[A]}{dx^2} \tag{D.1}$$

$$\frac{d[A]_{x=0}}{d[B]_{x=0}} = \exp\left(\frac{nF}{RT}(E(t) - E_c^{\Theta'})\right) \tag{D.2}$$

Where $[B]_{x=0}$ is the concentration of the reduced molecule at the electrode surface, $E(t)$ is the applied potential and $E_c^{\Theta'}$ the formal reverse potential, t is time, n is the number of electrons transferred per molecule of A reacting at the electrode surface, F is the Faraday constant, R the constant for an ideal gas, and finally T is the absolute temperature.

Nernst's law as described in Equation (D.2) approximates the ratio of the oxidized to the reduced molecule at the surface of an electrode when applying a certain potential. Nernst's law applies only to Nernstian reactions, which are electrochemically reversible redox reactions. The mechanism of GOx is considered a Nernstian reaction.

Using these laws, the bulk and surface concentrations can be related. Which allows the determination of the bulk concentration [22] as a function of the current over time.

$$[A]_{x=0} = [A]_{bulk} + \frac{1}{nFA\sqrt{D}}\frac{d^{-\frac{1}{2}}I(t)}{dt^{-\frac{1}{2}}} \tag{D.3}$$

$$[B]_{x=0} = \frac{1}{nFA\sqrt{D}}\frac{d^{-\frac{1}{2}}I(t)}{dt^{-\frac{1}{2}}} \tag{D.4}$$

Where the current flowing between the counter and working electrode $I(t)$ is given by

$$I(t) = -nFA\sqrt{D}\frac{d^{-\frac{1}{2}}}{dt^{-\frac{1}{2}}}\left(\frac{1}{1+\exp\frac{nF}{RT}(E_0 - vt - E_c^{\Theta\prime})}\right) \tag{D.5}$$

Where E_0 is the initial potential applied and v is the scan rate. The resulting current equation (D.5) is a linearly swept modification of the Cottrel equation given by

$$I(t) = \frac{nFAD^{1/2}C_0}{\pi^{1/2}t^{1/2}} \tag{D.6}$$

Where A is the electrode area (which varies over time because of bio-fouling) and C_0 is the bulk concentration of the electrically active chemical.